ESC-2004-081

Project Report
HTAP-21

Examples of EO-1 Hyperion Data Analysis

M.K. Griffin
S.M. Hsu
H-h.K. Burke
S.M. Orloff
C.A. Upham
B. Misra

12 January 2005

Lincoln Laboratory
MASSACHUSETTS INSTITUTE OF TECHNOLOGY
LEXINGTON, MASSACHUSETTS

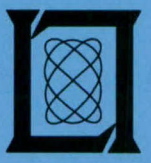

Prepared for the Department of the Under Secretary of Defense, S&T,
under Air Force Contract F19628-00-C-0002.

This report is based on studies performed at Lincoln Laboratory, a center for research operated by Massachusetts Institute of Technology. This work was sponsored by the Department of the Under Secretary of Defense, S&T, under Air Force Contract F19628-00-C-0002.

This technical report has been reviewed and is approved for publication.

FOR THE COMMANDER

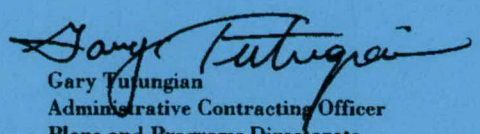

Gary Tutungian
Administrative Contracting Officer
Plans and Programs Directorate
Contracted Support Management

Massachusetts Institute of Technology
Lincoln Laboratory

Examples of EO-1 Hyperion Data Analysis

M.K. Griffin
S.M. Hsu
H-h.K. Burke
S.M. Orloff
C.A. Upham
Group 97

B. Misra
Group 48

Project Report HTAP-21

12 January 2005

Lexington Massachusetts

ABSTRACT

The EO-1 satellite is part of NASA's New Millennium Program (NMP). It consists of three imaging sensors: the multispectral Advanced Land Imager (ALI), Hyperion, and Atmospheric Corrector. Hyperion provides a high-resolution hyperspectral imager capable of resolving 220 spectral bands (from 0.4 to 2.5 micron) with a 30-m resolution. The instrument images a 7.5 km by 100 km land area per image. Hyperion is currently the only space-borne HSI data source since the launch of EO-1 in late 2000.

A cloud-cover detection algorithm was developed for application to EO-1 Hyperion hyperspectral data. The algorithm uses only bands in the reflected solar spectral regions to discriminate clouds from surface features and was designed to be used on board the EO-1 satellite as part of the EO-1 Extended Mission Phase of the EO-1 Science Program. The cloud-cover algorithm uses only 6 bands to discriminate clouds from other bright surface features such as snow, ice, and desert sand. The technique was developed using 20 Hyperion scenes with varying cloud amount, cloud type, underlying surface characteristics, and seasonal conditions. Results from the application of the algorithm to these test scenes are given with a discussion on the accuracy of the procedure used in the cloud cover discrimination. Compared to subjective estimates of the scene cloud cover, the algorithm was typically within a few percent of the estimated total cloud cover.

The unique capability of hyperspectral sensing is well-suited to coastal characterization: (1) most ocean feature algorithms are semi-empirical retrievals, and HSI has all spectral bands to provide legacy with previous sensors and to explore new information; (2) coastal features are more complex than those of deep ocean, and coupled effects are best resolved with HIS; and (3) with contiguous spectral coverage, atmospheric compensation can be done with more accuracy and confidence, especially since atmospheric aerosol effects are the most pronounced in the visible region where coastal features lie. To demonstrate the potential value of Hyperion (and HSI in general) data to coastal characterization, EO-1 data from Chesapeake Bay from 19 February 2002 are analyzed. It is first illustrated that hyperspectral data inherently provide more information for feature extraction than multispectral data provide although Hyperion has lower SNR than ALI. Chlorophyll retrievals are also shown. The results compare favorably with data from other satellite and aircraft data sources.

Finally, to demonstrate additional utility of EO-1 data, combined analysis of panchromatic, multispectral (ALI, Advanced Land Imager) and hyperspectral (Hyperion) data is conducted. Data sets from Coleambally Irrigation Area, Australia, on 7 March 2000 and San Francisco Bay area on 17 January 2000 are employed for the analysis. For terrain characterization, various indices are used: normalized vegetation index, plant liquid water index, and soil moisture index. Various fields are delineated according to their moisture and vegetation states. Spectral unmixing of soil and vegetation is illustrated. Anomaly detection of distinct roof material is also shown.

ACKNOWLEDGMENTS

This work was part of the Hyperspectral Technology Assessment Program (HTAP) sponsored by DUSD (S&T). The authors wish to express their gratitude to CAPT Frank Garcia and Lt. Col. Karl Dahlhauser for their support.

Part of the work (cloud-cover analysis) was sponsored by the NASA EO-1 Extended Mission program. We want to thank Bruce Trout at Microtel and Dan Mandl, Jerry Miller, Stuart Frye, and Lawrence Ong at NASA/GSFC for their interactions throughout this program, and Dr. Steve Ungar of NASA, EO-1 Project Scientist, for his initial support of the cloud-cover effort.

Another portion of the work (coastal characterization) is also part of the NOAA GOES Program conducted at MIT Lincoln Laboratory and sponsored by NOAA NESDIS. The authors wish to acknowledge the guidance from, and valuable discussions with, Dr. Edward Howard and Mr. John Pereira, both of NOAA NESDIS.

TABLE OF CONTENTS

LIST OF ILLUSTRATIONS

LIST OF TABLES

1. INTRODUCTION

Hyperspectral imaging (HSI) sensors have been used for more than a decade to aid in the detection and identification of diverse surface targets and topographical and geological features. Techniques for scene characterization can utilize individual or combinations of spectral bands to identify specific features in an image. Three examples of surface characterization demonstrating utilities of the EO-1 sensor data are included in this report.

The first example deals primarily with the problem of discrimination of clouds from surface features. A simplified cloud detection algorithm was developed that utilizes only reflected solar measurements from the EO-1 Hyperion sensor to discriminate clouds from all other features in the image (Griffin, et al., 2003). This cloud detection effort was part of the EO-1 Extended Mission Phase of the EO-1 Science Program. The overall effort was designed to demonstrate the potential for performing cloud cover detection on board the satellite to regulate which scenes would be transmitted for ground processing. The effort involved retrieving a collected Hyperion image into onboard memory, calibrating the image data to Level-1B radiances, converting the radiances to at-sensor or top-of-the-atmosphere reflectances and performing the cloud cover detection. The last two steps of this process: conversions of radiance to reflectance and cloud cover detection are described here. This work represents the first time that an application such as cloud detection is to be performed on-board a space-borne sensor.

The second example demonstrates the potential value of Hyperion (and HSI in general) data to coastal characterization. Oceans comprise two-thirds of the Earth's surface. Remote sensing provides the only reasonable way of monitoring and understanding this majority part of our planet. Optical properties of natural bodies of ocean water are influenced by many factors. Some of the key substances affecting ocean characteristics are phytoplankton, suspended material, and organic substances. Spectral remote sensing provides a means of routinely obtaining information of the ocean status (IOCCG #1, 1998; IOCCG #2, 1999; IOCCG #3, 2000). EO-1 data from Chesapeake Bay from 19 February 2002 are analyzed. Hyperion data are first compared with multispectral ALI data to gain insights of the additional information content of hyperspectral data. A simple algorithm for chlorophyll retrieval is also applied. The results compare favorably with data from other sources.

In the third example, a combined analysis of panchromatic, multispectral (ALI), and hyperspectral (Hyperion) data is shown to demonstrate additional utility of EO-1 data for terrain characterization, anomaly detection and feature extraction, and spectral unmixing. Data sets from Coleambally Irrigation Area, Australia, on 7 March 2000 and the San Francisco Bay area on 17 January 2000 are employed for the analysis. Various tools for terrain analysis to delineate and characterize vegetation and soil are applied. These soil and vegetation fields are further clustered as their spectral characteristics vary. Application of an anomaly detection algorithm successfully identified distinct roof material.

1.1 Hyperion Sensor

The NASA New Millennium Program's Earth Observing -1 Satellite (NMP EO-1) was successfully launched on 21 November 2000. There are three primary instruments on the EO-1 spacecraft: the Advanced Land Imager (ALI), Hyperion, and the Linear Etalon Imaging Spectrometer Array (LEISA) Atmospheric Corrector (LAC). The EO-1 platform was positioned on orbit to be approximately one minute behind the Landsat 7 sensor at an altitude of 705 km (Pearlman, et al., 2001). With the demise of the Lewis and Orbiview-4 spacecrafts, EO-1 uniquely offers a space-borne spectral imaging capability that is not currently available from any other source (HTTP://EO1.USGS.GOV/). The essential spatial and spectral characteristics of the EO-1 instrument suite in comparison to Landsat 7 are summarized in Table 1-1. The overlap in coverage of the ALI, Hyperion, and LAC, compared to the Landsat 7 ground track is shown in Figure 1-1 (Ungar, 2002).

ALI consists of a 15° Wide-Field Telescope (WFT) and partially populated focal plane occupying 1/5th of the field of view, giving a ground swath width of 37 km. The Advanced Land Imager (ALI) was designed to be a Landsat follow-on type of sensor with similar bands and spatial resolution to the Landsat 7 sensor. Hyperion is a grating imaging spectrometer providing 10-nm (sampling interval) contiguous bands in the solar reflected spectrum from 400–2500 nm with a spatial resolution of 30 meter (the same as the ALI and Landsat sensors) over a 7.7-km swath. Each swath or line of data contains 256 pixels. LAC is an imaging spectrometer covering the spectral range from 900 to 1600 nm, but with a spatial coverage in the 100's of meters to monitor the atmospheric water absorption lines for correction of atmospheric effects in multispectral imagers.

Table 1-1 EO-1 Instrument Overviews

Parameters	Landsat 7	EO-1	EO-1	
	ETM+	ALI	HYPERION	AC
Spectral Range	0.4-2.4 μm*	0.4-2.4 μm	0.4-2.5 μm	0.9-1.6 μm
Spatial Resolution	30 m	30 m	30 m	250 m
Swath Width	185 Km	37 Km	7.7 Km	185 Km
Spectral Resolution	Variable	Variable	10 nm	3-9 nm**
Spectral Coverage	Discrete	Discrete	Continuous	Continuous
Pan Band Resolution	15 m	10 m	N/A	N/A
Number of Bands	7	10	220	256

* Excludes thermal channel

** 35/55 cm^{-1} constant resolution

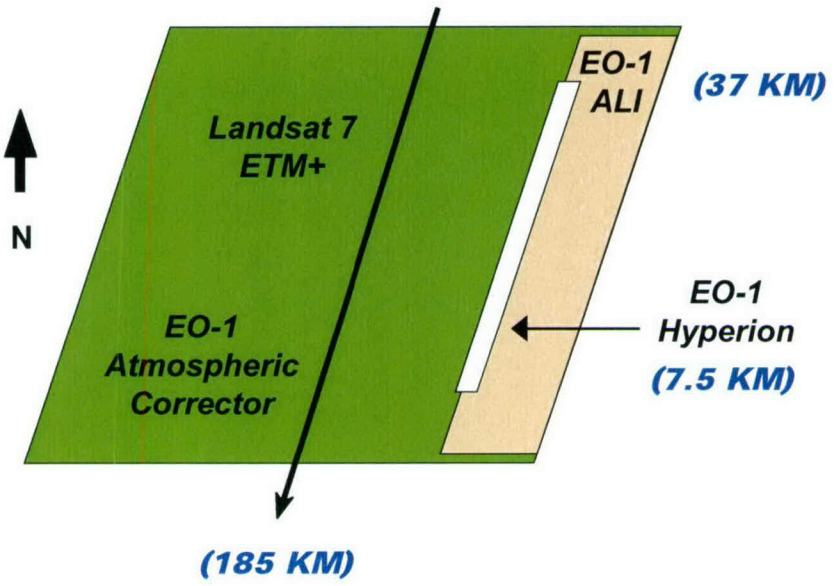

Figure 1-1 EO-1 and Landsat 7 instrument ground tracks. Hyperion is a pushbroom-imaging sensor with a swath width of 7.5 km. The EO-1 platform was positioned on orbit to be approximately 1 minute behind the Landsat 7 sensor at an altitude of 705 km.

2. HYPERION CLOUD-COVER ANALYSIS

This section deals primarily with the problem of discrimination of clouds from surface features. Most cloud detection or cloud mask schemes utilize both solar reflected (visible, near-infrared, and shortwave infrared) and thermal emitted (midwave and longwave infrared) measurements (Ackerman, et al., 1998). LWIR data provides information as to the physical temperature of the cloud and the surface, a useful discrimination tool. Reflected solar measurements, which are common to many HSI sensors, rely primarily on spectral reflectance differences to discriminate scene features. A simplified cloud detection algorithm has been developed that utilizes only reflected solar measurements from the EO-1 Hyperion sensor to discriminate clouds from all other features in the image (Griffin, et al., 2003).

2.1 Algorithm Description

The Hyperion Cloud-Cover algorithm utilizes only six Hyperion bands to discriminate all types of clouds from other surface features in a scene. The selection of the six bands provided spectral information at critical wavelengths while keeping processing costs to a minimum. This was a key aspect of the entire cloud-cover detection process since both onboard computer memory and processing time were limited. The six bands chosen for the initial form of the cloud-cover algorithm are given in Table 2-1. They include two visible channels, a near-IR channel and three SWIR channels.

Table 2-1. Hyperion Bands Used in the Cloud-Cover Algorithm

Band (μm)	Usage
0.55	Snow/ice/cloud test
0.66	Red reflectance test Vegetation ratio test
0.86	Vegetation ratio test Desert/sand test
1.25	Snow/ice/cloud test Desert/sand test
1.38	High cloud test Ice/low cloud test
1.65	Snow/ice/cloud test Desert/sand test

Hyperion has two detectors: the first covers the visible and near-IR while the second covers the SWIR bands. The current algorithm requires channels from both detectors. An algorithm using only visible and near-IR bands was considered but cloud-cover detection results were not good for scenes with bright surfaces (desert, snow, ice). Utilizing these six channels, formulas have be adapted or developed relating the spectral

measurements to discriminate and identify cloud features in a scene. Figure 2-1 provides a flowchart of the Hyperion cloud-cover algorithm. A brief description of the phenomenology behind the algorithm follows. Each test detailed below is designed to eliminate specific non-cloud features for promising cloud pixels.

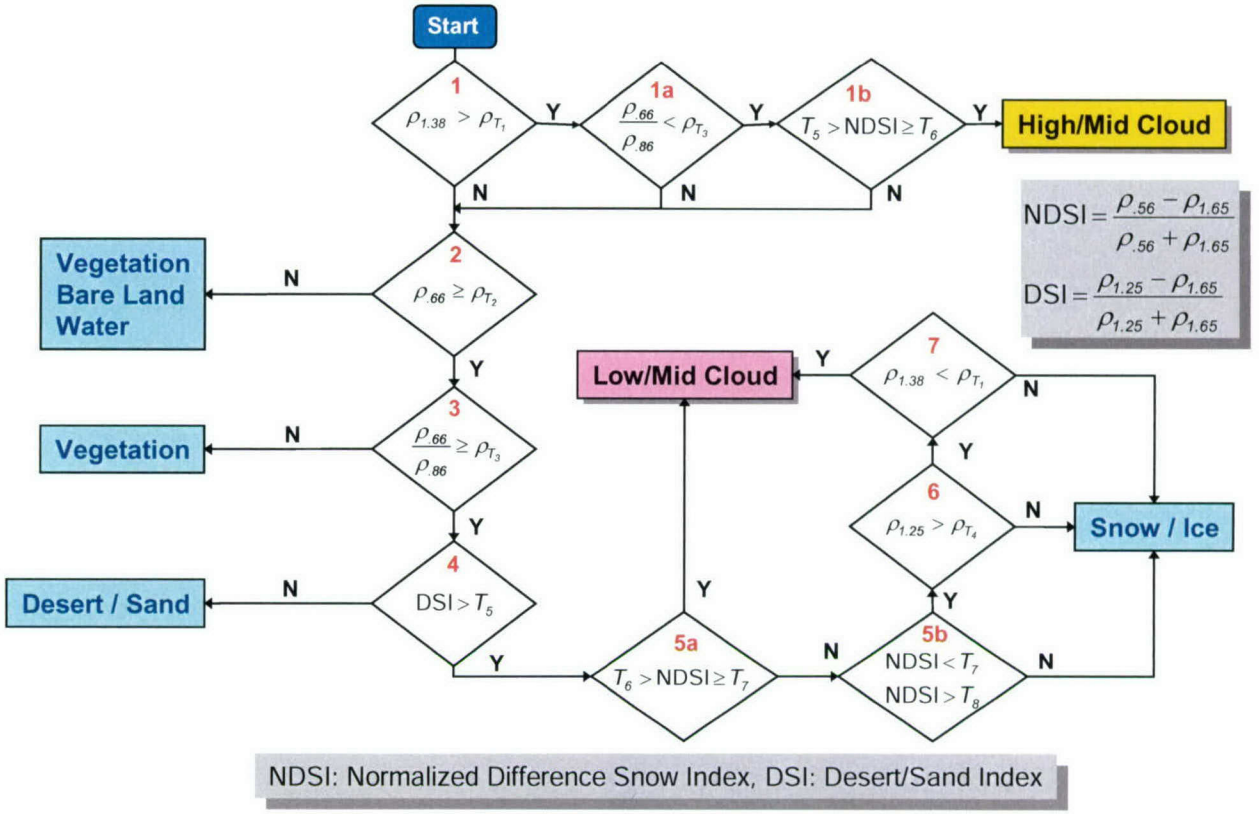

Figure 2-1 Flowchart of the cloud-cover detection process

2.1.1 *Conversion of radiance to reflectance*

Channels with center wavelengths up to 3 μm derive their signal from reflected solar energy off land, water, and cloud features. The amount of solar energy that is reflected provides information about surface and atmospheric feature characteristics such as absorption and scattering properties. The reflectivity of an object in a scene is generally not a function of the incident solar insolation (although it is a function of the viewing geometry). Therefore, deriving the apparent or at-sensor reflectivity for a scene can remove the variation in the solar illumination with wavelength.

For the Hyperion sensor, where reflected solar flux is the primary illumination source, it is useful to convert the channel radiance L_i to an *at-sensor* reflectance ρ_t. This can be accomplished by dividing the channel radiance by the incident solar flux $F_{0,i}$ corrected for sun angle μ_0 and earth-sun distance $d_{e\text{-}s}$ (in *Astronomical Units, AU*),

$$\rho_i = \left(\frac{\pi}{\mu_0 F_{0,i} / d_{e-s}^2} \right) L_i \quad . \tag{2-1}$$

The sun angle is defined by $\mu_0 = \cos(\theta_0)$, where θ_0 is the solar zenith angle. The solar zenith angle may be obtained through the EO-1 telemetry or it can be calculated from the measurement date, time of day and geographical location. The earth-sun distance measure $d_{e\text{-}s}$ adjusts the mean solar flux $F_{0,i}$ for orbital radius changes. The earth-sun distance is a function of the Julian day and is computed using a parameterized function of the actual earth-sun distance variation.

The incident solar flux as a function of wavelength $F_0(\lambda)$ can be obtained from a number of sources; the MODTRAN radiative transfer model (Berk, et al., 1998) contains a solar illumination database which can be easily adapted to the computation in the above equation. The solar flux must be convolved with the Hyperion band spectral response functions to obtain the channel solar flux F_{0i}. Equation (2-1) is then applied to each band radiance image to obtain an equivalent set of reflectance images.

Hyperion measurements are distributed as scaled radiance. True radiance is obtained by dividing the scaled radiance by a factor (either 40 or 80) based upon the channel number. Hyperion radiances are archived in units of $W/m^2\text{-}sr\text{-}\mu m$. The popular unit of radiance for hyperspectral and other applications is the *μflick* ($\mu W/cm^2\text{-}sr\text{-}\mu m$), which can be obtained by multiplying the Hyperion radiance values by 100.

2.1.2 *High clouds*

High clouds typically have spectral reflectance characteristics that are similar to other cloud types. However, high, thin, predominantly ice clouds are generally not opaque to underlying surface reflectance, such that surface features can be observed through the clouds. This adds a level of difficulty in detecting high clouds, especially if LWIR information is not available. Techniques using observations in the strong water vapor absorption bands have provided a new method to discriminate high clouds from

low clouds and surface features (Gao and Kaufman, 1995; Gao, et al., 1998). At these wavelengths the water-vapor absorption is typically strong enough to completely suppress the contribution from both the reflectance from the surface and low-altitude clouds while adequately transmitting radiation scattered from high-altitude clouds. This allows the possibility for discriminating high clouds from lower-altitude clouds and surface features using only a simple reflectance threshold test.

However, in polar latitudes or at high elevations, the amount of moisture in the atmosphere is greatly reduced, resulting in reduced water vapor absorption in the 1.38 μm band. This increases the penetration of observations at these wavelengths and increases the possibility of some significant surface reflectance contribution to the signal. For these cases, bright surface features (snow or ice) may be mistaken for high clouds and further testing is required to discriminate these features. A band ratio test is applied to eliminate ice surfaces and the Normalized Differential Snow Index (NDSI) is used to eliminate snow features. Both tests are also used later on in the processing and are described in more detail below. All pixels that are not flagged as high cloud are passed on for further testing.

2.1.3 Reflectance at 0.66 μm

Clouds are typically one of the brightest features in a Hyperion image. The reflectance from clouds is nearly invariant in the visible and near-IR window regions since the size of the scatterers in the cloud are much larger (size parameter >> 1) than the sensor wavelengths. This information can be used to discriminate clouds from darker background objects and from bright but spectrally variable surface features.

In the visible spectral band, dark surface objects can be distinguished from bright clouds by a simple reflectance threshold test. At 0.66 μm, many surface features such as water, vegetation, shadowed areas, and soil exhibit low reflectance values (< 0.15) and can be easily flagged. Pixels that fail (< threshold) this test are flagged clear; all other pixels are passed on for further testing. Errors with this test can occur for low sun conditions, which can reduce the cloud reflectance, or for some types of clouds (i.e., cumulus), which can self-shadow.

2.1.4 Vegetation index ratio

Vegetated surfaces exhibit a strong reflectance gradient near 0.7 μm, known as the *red edge* (Tucker, 1979). The reflectance for vegetation changes from ~ 0.1 in the visible to 0.4 or greater in the NIR depending on specific aspects of the vegetation cover (health, greenness, etc.). Clouds on the other hand display a nearly constant reflectance signal over this range. Therefore, a ratio of a visible to a NIR channel should be close to 1 for clouds and less than 0.5 for vegetated surfaces. In general, clouds have slightly less reflectance in the visible than in the NIR. Snow and ice surfaces have a similar behavior to clouds in this spectral region. Figure 2-2 provides an example of Hyperion reflectance values for clouds, vegetation and surface ice where the previously mentioned relationships can be observed.

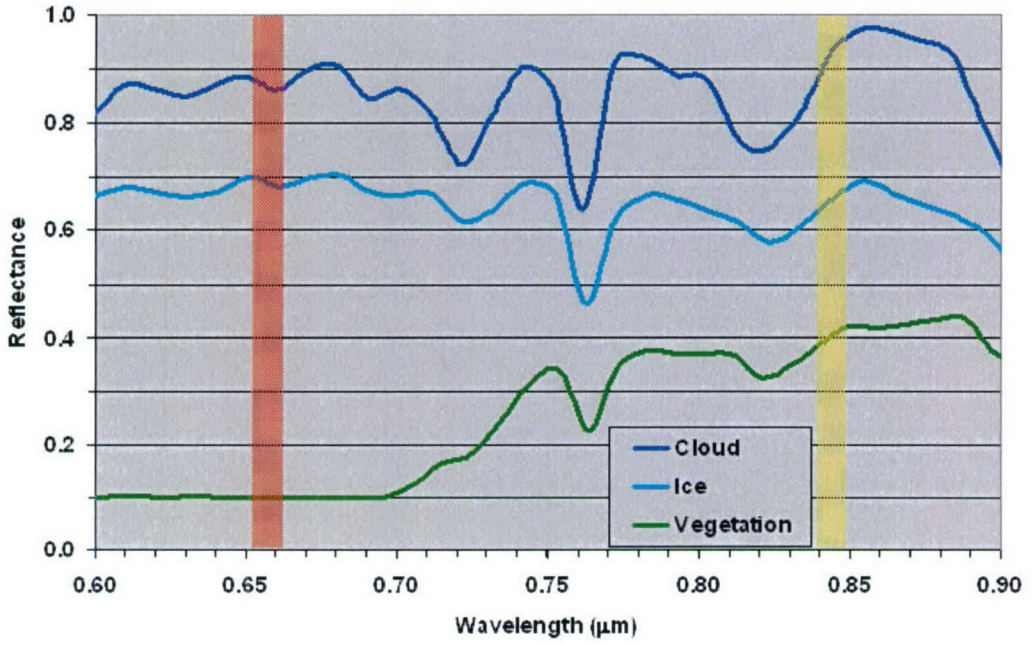

Figure 2-2 Plot of the spectral signatures of three features in the visible and NIR: clouds, surface ice, and vegetation. The red and orange vertical lines represent locations of the visible and NIR bands, respectively, used in the vegetation index ratio test.

2.1.5 Desert sand index

Bright surface features such as snow, ice, and sand can easily be mistaken for cloud features in the visible portion of the spectrum. It is important to be able to distinguish bright surface features from similarly bright clouds. Desert sand is composed of numerous minerals including quartz, which strongly reflect sunlight. In contrast to other bright surface features such as snow and ice, desert sand tends to display the largest reflectance near 1.6 μm, whereas snow and ice show peaks in the visible and NIR. Clouds also tend to display higher reflectance values in the NIR with a noticeable drop in reflectance in the SWIR. These observations provide an empirical means to formulate a discrimination index, or Desert Sand Index (DSI), similar to vegetation indices. The DSI was derived to highlight the change from low to high reflectance in the visible and near-IR spectral region for desert and sand surface types. It uses the change in reflectance from the NIR to the SWIR as shown in the formula below,

$$DSI = \frac{\rho_{0.86} - \rho_{1.65}}{\rho_{0.86} + \rho_{1.65}}. \tag{2-2}$$

In Figure 2-3, plots of the Hyperion-observed spectral reflectance for snow, ice, desert, and cloud features are shown. Comparing values near the red (0.86 μm) and orange (1.65 μm) vertical bands shows that the sand feature is the only one that will display a negative DSI value. This provides a process for eliminating bright sand and desert surfaces from consideration as cloud.

2.1.6 *Normalized snow index*

The Normalized Difference Snow Index (NDSI) is used to identify snow- and ice-covered surfaces and for separating snow/ice and cumulus clouds. The NDSI measures the relative difference between the spectral reflectance in the visible and SWIR. The technique is analogous to the normalized-difference vegetation index (NDVI), which provides a measure of the health and greenness of vegetated surfaces (Tucker, 1979). The formula commonly used for the NDSI is given by,

$$NDSI = \frac{\rho_{0.56} - \rho_{1.65}}{\rho_{0.56} + \rho_{1.65}}. \tag{2-3}$$

NDSI values greater than approximately 0.4 are representative of various snow-covered conditions with pure snow having the highest NDSI values. The NDSI tends to decrease as other features (such as soil and vegetation) are mixed in with the snow.

2.1.7 *Reflectance at 1.25 μm*

Some moderately bright surface features (such as aged or shadowed snow) may fail the NDSI test. Many of these features can be eliminated from consideration as cloud by comparing their reflectance at 1.25 μm to an empirically defined threshold. Most surface features have reflectance values less than 0.4 at this wavelength while clouds still display reflectances greater than 0.4 (see Fig. 2-3). The 1.25-μm reflectance test is applied only to potential cloudy pixels that have survived previous tests.

2.1.8 *Ice discrimination*

To further discriminate ice surfaces from water-cloud pixels, pixels that have reflectance values at 1.37 μm greater than 0.1 are assumed to be ice surfaces and eliminated from consideration as cloudy. Referring to Fig. 2-3, it can be seen that for water clouds and bright snow-covered surfaces, reflectance values at 1.37 μm are quite low, much less than 0.1. Ice surfaces, however, display a significant reflectance signal at this wavelength. Since ice cover tends to occur during winter months when the air is normally quite dry, this surface feature can often be seen in the 1.37-μm water vapor band and can be mistaken for mid-high-level clouds.

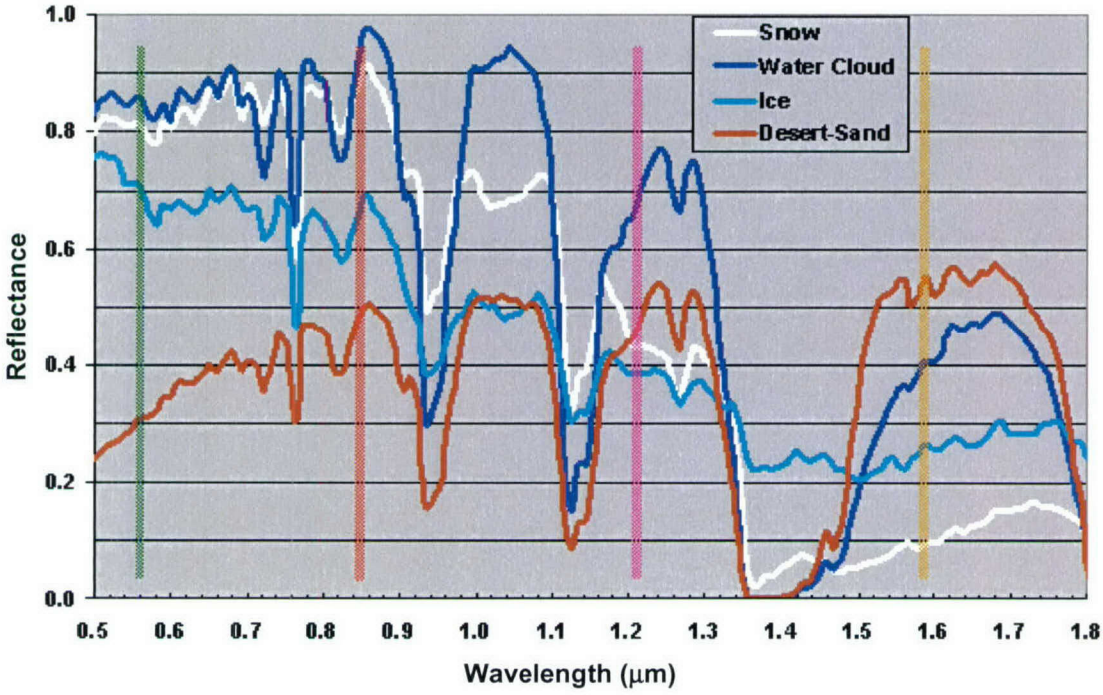

Figure 2-3 Plot of the spectral signatures for four features in the visible, NIR, and SWIR: clouds, surface ice and snow, and desert sand. The red and orange vertical bands represent locations of the NIR and SWIR channels, respectively, used in the desert sand index test. The green and orange bands represent channels used in the snow/ice discrimination tests.

2.2 Algorithm Applications

The cloud-cover detection process defined in Fig. 2-1 has been applied to a set of 20 Hyperion scenes with varying cloud cover and type, surface characteristics, and seasonal collection times. Each scene was converted from radiance to reflectance using the technique described in Section 2.1.1. The cloud-cover detection algorithm was applied independently to each pixel in a scene; effects from adjacent pixels did not influence the computation. While the tests described in Section 2.1 discriminate specific surface features from clouds, no attempt was made at this time to classify the surface features based upon the results from the tests. A simple cloud/no-cloud mask was provided as the primary output product along with line-by-line statistics of the presence of cloud-free pixels, water-cloud, and ice-cloud covered pixels. Examples of the Hyperion scenes that were used in the testing are shown below. An RGB rendition of the scene is shown along with the computed cloud mask. While full Hyperion scenes normally comprise over 3000 lines, only 1000 line subsets of each scene are shown for display purposes. The computed cloud amount for the 1000 line scene subset is given in the figure captions. For each of the cases below, the associated figure depicting the cloud cover uses the following color scheme: blue – cloud-free, gray/maroon – low/mid cloud, orange – mid/high cloud.

2.2.1 Kokee, Hawaii

This scene was collected on 22 May 2002 at 2056 UTC over the island of Kauai, HI. The scene is characterized by partly cloudy conditions with cumulus clouds present over land and water (Fig. 2-4). Clear regions are also visible. The algorithm does well detecting clouds over the land; over the water the main cloud region is masked, but some areas of thin cloud cover may not be identified. The 0.66-μm threshold reflectance test is the predominant test used over the water for non-ice clouds. Adjusting the threshold value would allow the capture of more clouds over the water. Over the land area, both the reflectance and ratio tests are primarily used to discriminate the clouds from underlying vegetation. The routine seems to miss a small amount of cloud cover over land, mostly cloud edges, which would support a slight reduction in the threshold value for the reflectance test. The total computed cloud amount for this scene segment is 41.3%, which appears to underestimate the actual cloud cover by, at most, a few percent.

2.2.2 Cheyenne, Wyoming

This scene was collected on 5 March 2002 at 1720 UTC near Cheyenne, WY. The scene is characterized by partly cloudy conditions with high, thin clouds overlying snow-covered hilly terrain (Fig. 2-5). The visible clouds are identified as mid-high-level clouds by the 1.38-μm threshold reflectance test. The clouds are thin enough that some of the underlying terrain is visible, especially near the bottom of the scene. The NDSI test accurately identifies the bright snow-covered terrain as a surface feature with the possible exception of some areas near the edge of the high clouds. Here, the snow-covered surface is masked as a low-mid cloud. These areas seem to be shadowed either by the high clouds or self-shadowed due to terrain variations and the moderate sun elevation (36 degrees above the horizon). These regions of possible misidentification comprise only a small percentage of the image (< 4 %). The overall computed cloud amount for the scene is 58.9%, which appears to be a slight overestimate in this case.

2.2.3 Kansas City

The scene depicted in Fig. 2-6 was collected near Kansas City, KS, on 4 March 2002 at 1638 UTC. The image is characterized by thin mid-level clouds overlying snow-covered terrain. Some river and road features are observable. The algorithm correctly identifies all of the thin cloud cover, but also misidentifies apparently clear areas as cloud as well. These areas are located in the upper right quadrant of the image. As with the Cheyenne, WY, scene, these seem to be areas of darker snow-covered terrain. The algorithm fails to identify these regions as snow since the NDSI values fall below the nominal threshold for snow. Further tests do not eliminate these features and they are identified as low/mid cloud. For this case the amount of clear land that is misidentified as cloud is approximately 3 – 7%. The overall computed cloud cover for this scene is 72.6% and appears to be an overestimate by about 5%.

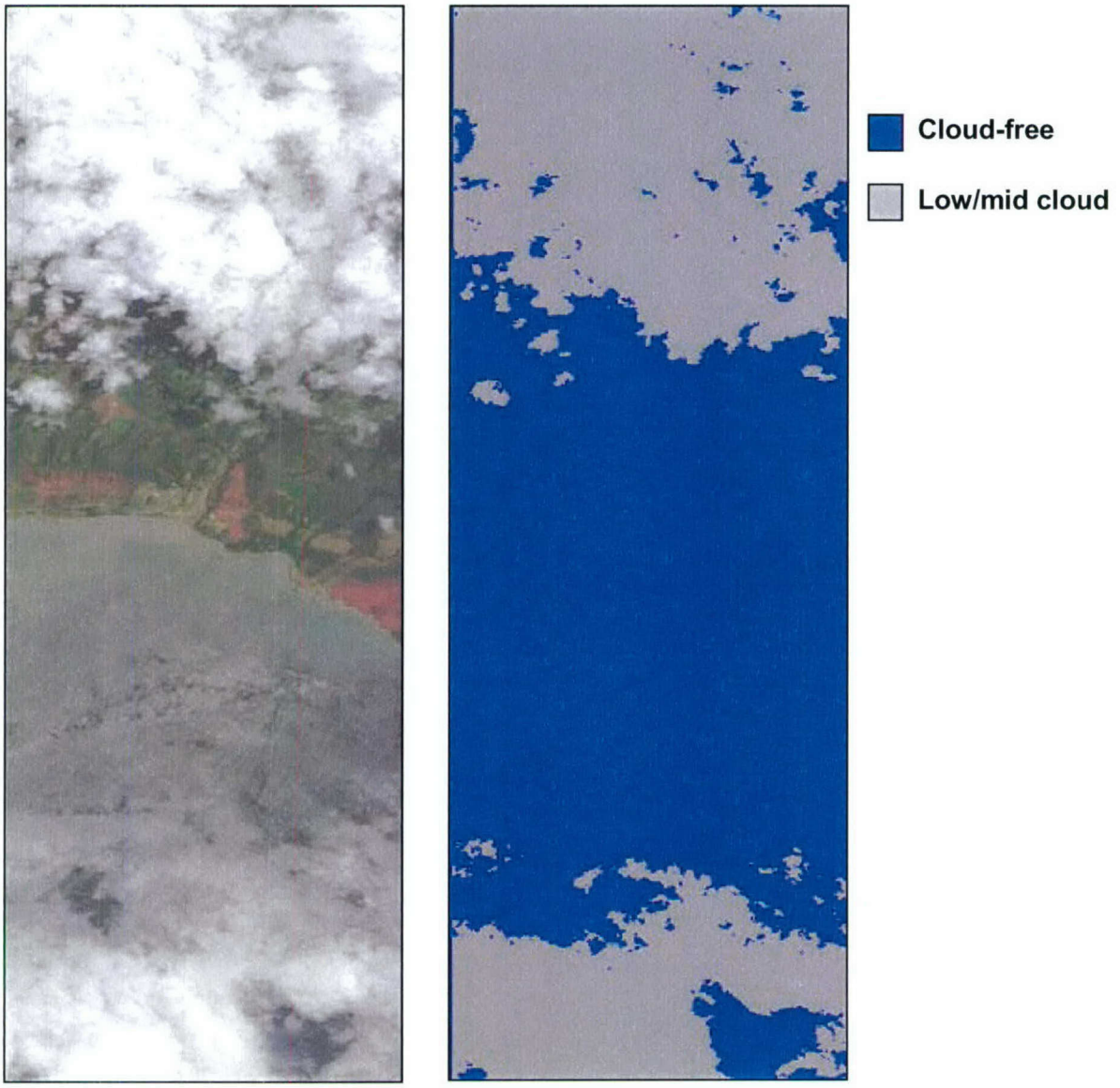

Figure 2-4 Hyperion image collected over Kauai, HI, displaying partly cloudy conditions with cumulus clouds over land and water. The scene was taken on 22 May 2002 at 2056 UTC. The algorithm computed the cloud amount for the scene to be 41.3%.

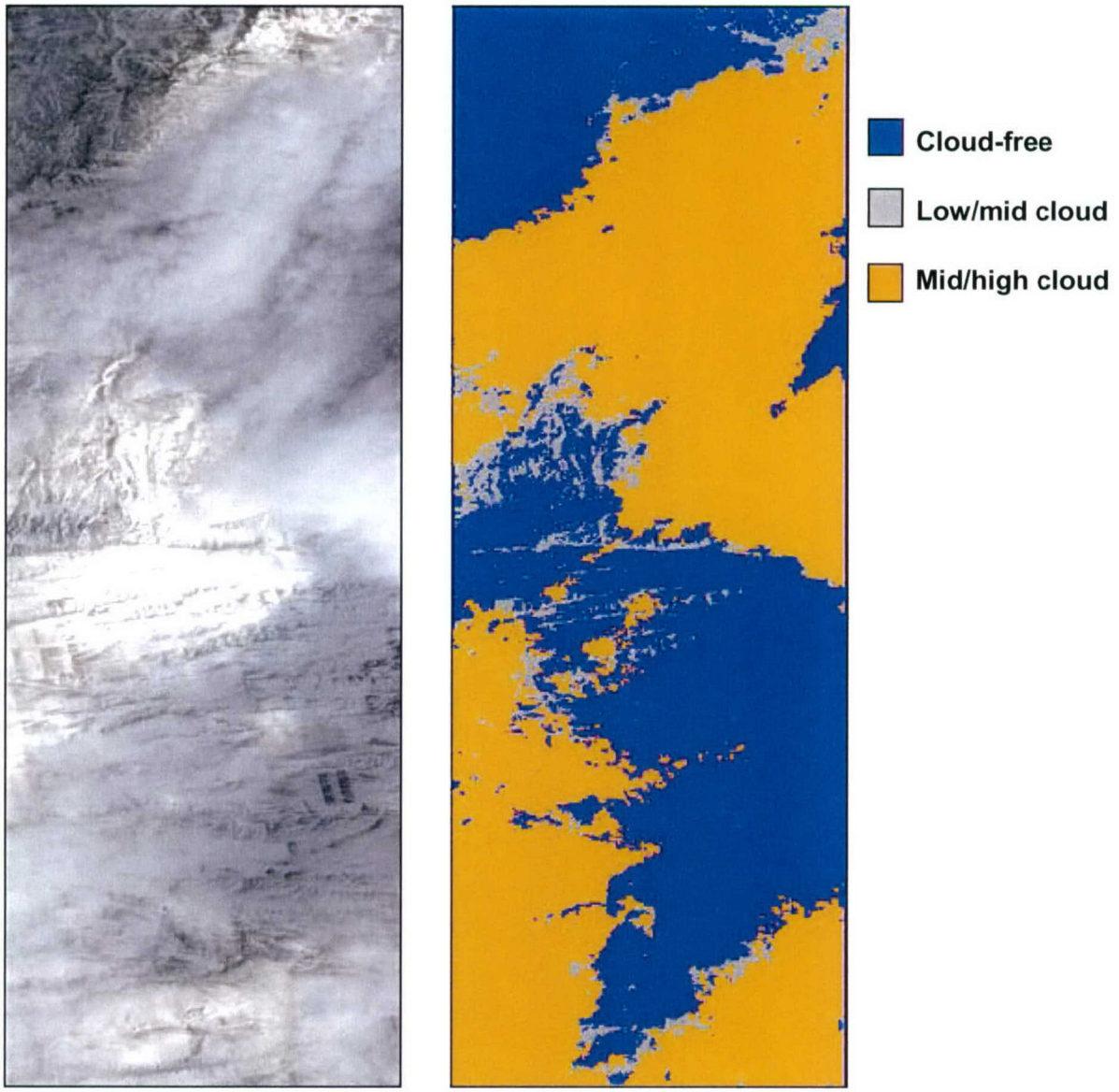

Figure 2-5 Hyperion image collected near Cheyenne, WY, displaying partly cloudy conditions with high thin clouds over snow-covered hilly terrain. The scene was taken on 5 March 2002 at 1720 UTC. The algorithm computed the cloud amount for the scene to be 58.9%.

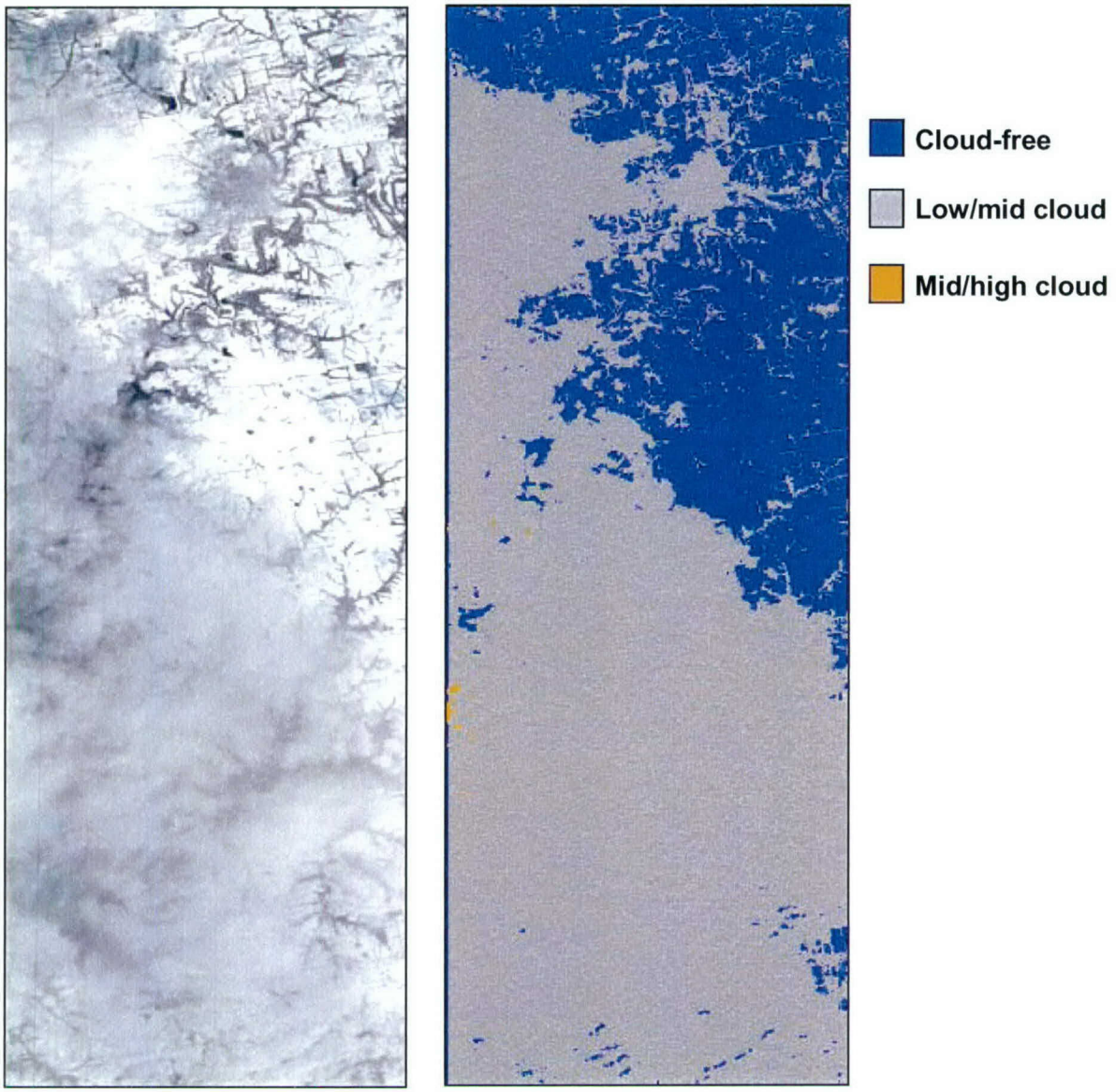

Figure 2-6 Hyperion image collected near Kansas City, KS, displaying partly cloudy conditions with thin mid-level clouds over snow-covered terrain. The scene was taken on 4 March 2002 at 1638 UTC. The algorithm computed the cloud amount for the scene to be 72.6%.

2.2.4 Chiefs Island

This scene was collected on 16 April 2002 at 0821 UTC near Chiefs Island, South Africa. Various types of cumulus clouds are present (see Fig. 2-7). The algorithm does an adequate job of identifying the majority of the cloud fields although some of the cloud street patterns near the center of the image are missing from the cloud mask. The 0.66-μm reflectance test is predominantly used to identify these types of clouds and a lowering of the threshold might improve the cloud cover detection. The overall computed cloud amount for this image is 68.9%, which seems to be an underestimate by about 5–7%.

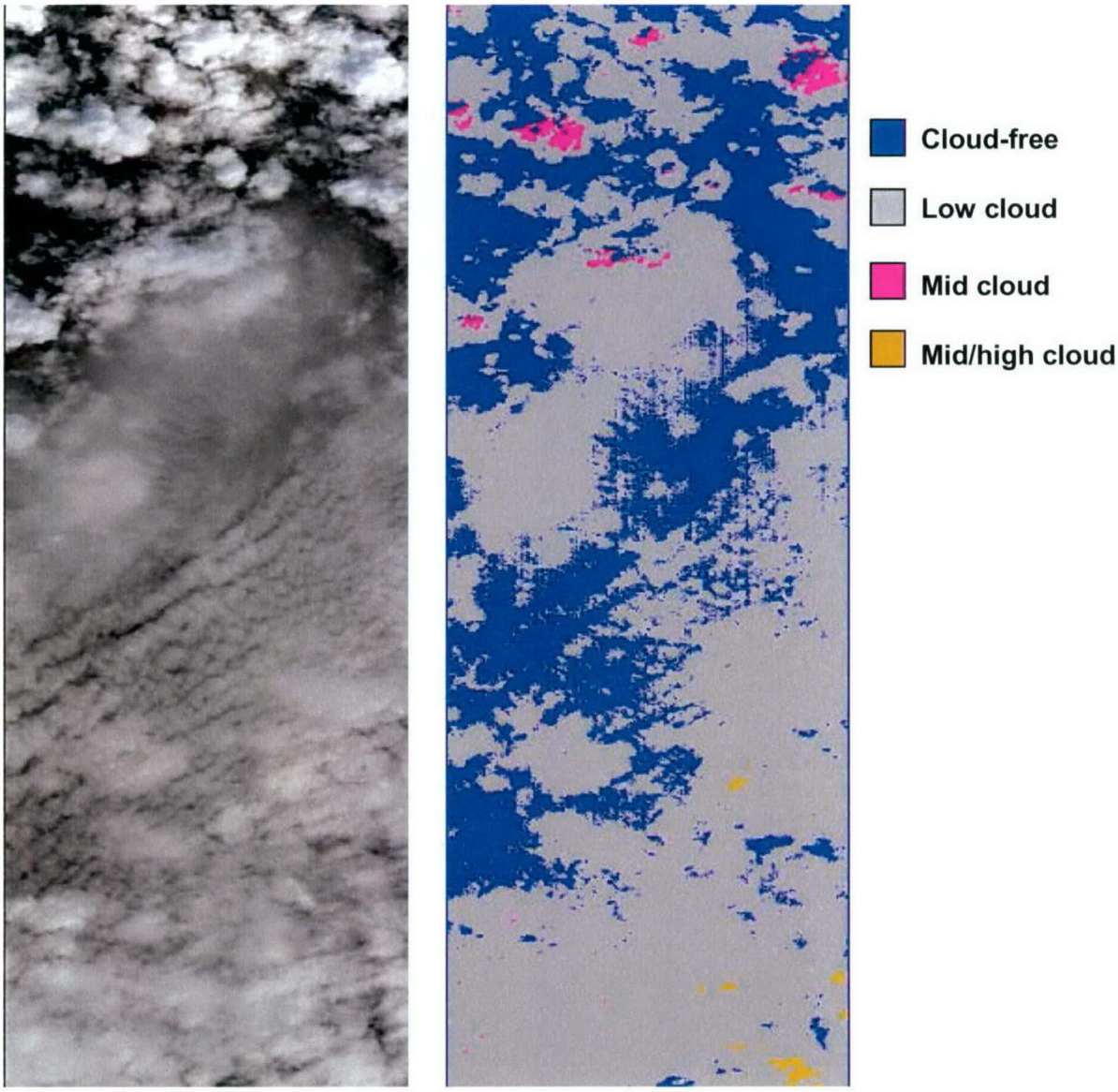

Figure 2-7 Hyperion image collected near Chiefs Island, South Africa, displaying mostly cloudy conditions with a variety of cumulus cloud fields present. The scene was taken on 16 April 2002 at 0821 UTC. The algorithm computed the cloud amount for the scene to be 68.9%.

2.2.5 Bering Sea

The scene depicted in Fig. 2-8 was collected in the Bering Sea on 20 April 2002 at 2318 UTC. This is one of a number of clear scenes over bright surfaces that were chosen to test the ability of the algorithm to discriminate bright surface features from clouds. In this case the scene is predominantly snow-covered ice and land with a coastline feature running horizontally across the center of the image with ice towards the bottom of the image. Some road and structure features are apparent near the center of the image. The algorithm does an excellent job identifying the snow and ice features as cloud-free. A

small amount of the dark features in the upper part of the image were misclassified as cloud; the computed cloud amount for this image was 0.7%.

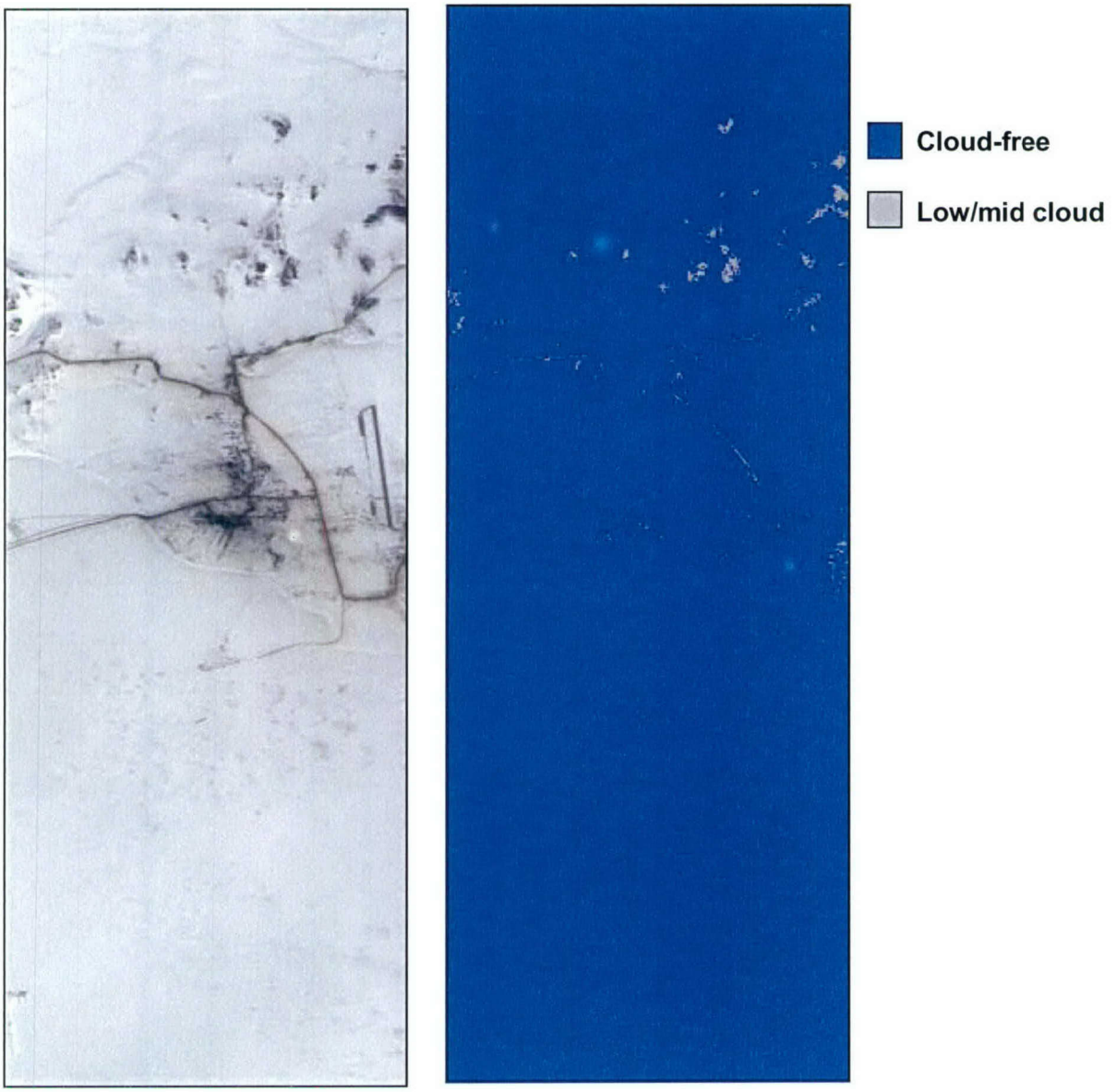

Figure 2-8 Hyperion image collected in the Bering Sea, displaying clear conditions over both snow-covered ice and land. The scene was taken on 20 April 2002 at 2318 UTC. The algorithm computed the cloud amount for the scene to be 0.7%.

2.2.6 Suez Canal

The scene depicted in Fig. 2-9 was collected over the Suez Canal on 23 April 2002 at 0813 UTC. This region is characterized by bright sand and desert conditions. The Suez Canal is clearly observed, as is a ship in the canal near the center of the image. The Desert Sand Index does well to identify the bright regions of the image as surface

features. A small amount of the bright region in the lower part of the scene was identified as cloud. The computed cloud amount for this image was 0.3%.

Figure 2-9 Hyperion image collected of the Suez Canal, displaying clear conditions over a desert-type scene. The scene was taken on 23 April 2002 at 0813 UTC. The algorithm computed the cloud amount for the scene to be 0.3%.

2.3 Summary

A technique for estimating the cloud amount in a hyperspectral scene has been described. The algorithm was designed to perform cloud-cover detection on board the EO-1 satellite, an achievement which has never been accomplished before. The technique requires calibrated Level 1B radiances, which are converted to reflectance values and processed through the cloud-cover routine to produce a cloud mask for the observed

image. The routine was tested on numerous Hyperion images collected over a wide range of surface and atmospheric conditions.

The algorithm does remarkably well considering that no thermal infrared data is available to assist in the cloud-cover determination. A set of seven tests is used to discriminate surface features from clouds. Two types of clouds are identified in this routine: low/mid (water) and mid/high (ice) clouds. Tests of the routine produced cloud-cover estimates that were generally within 5% of the visually estimated cloud cover amount. The algorithm has the most difficulty with shadowed or darkened snow-covered surfaces that are not identified properly in the NDSI test.

The algorithm was uploaded and tested on board the EO-1 spacecraft in Spring 2003 and produced a successful cloud-cover estimate using a scene collected by the Hyperion sensor. The results supported the use of onboard cloud-cover computation for alternate scene selection, i.e., if the cloud cover estimate is greater than desired for a particular scene, then a decision can be made to collect a different scene on the next orbital pass. This would avoid the process of collecting, storing, transmitting to ground, and processing the scene only to find out that the scene is obscured by clouds and not usable.

3. REMOTE SENSING OF COASTAL WATERS

Oceans comprise two-thirds of the Earth's surface. Remote sensing provides the only reasonable way of monitoring and understanding this majority part of our planet. Optical properties of natural bodies of ocean water are influenced by many factors. Some of the key substances affecting ocean characteristics are phytoplankton, suspended material, and organic substances. In general, ocean waters are partitioned into Case 1 (open ocean) and Case 2 (coastal) waters. Case 1 waters are those in which phytoplankton are the principal agents responsible for variations in optical properties of the water. On the other hand, Case 2 waters are influenced not just by phytoplankton and related particles, but also by other substances, notably inorganic particles in suspension and yellow substances. Figure 3-1 is a representation of Case 1 and Case 2 waters according to their optical properties caused by phytoplankton (P), yellow substances (Y), and suspended material (S). Coastal waters are more complex in their composition and optical properties than open ocean waters are. Sensing requirements are more stringent and interpretation of data is also a challenge due to the following points (Burke, et al., 2003):

- Ocean color in coastal waters is influenced in a nonlinear fashion by a number of constituents in the water. In shallow waters, it is further influenced by the depth of the water column and by the nature of the bottom.
- Some of the inherent optical properties of the constituents that influence ocean color can be similar to each other. The similarity may persist over the entire spectral range of interest, as in the case of the absorption spectra of colored dissolved organic matter and detrital particles. Similarities impede differentiation of the substances by remote sensing.
- The concentrations of in-water constituents have wide dynamic ranges. For example, chlorophyll-a concentration varies over several orders of magnitude, from about 0.01 to 100 mg m^{-3}.
- Each of the three major components of the water that influence ocean color in Case 2 waters (phytoplankton, other suspended particulates, and yellow substances) represents a group of substances rather than a single substance. A consequence is the variability in their optical signatures.

These are points that have to be kept in mind when developing algorithms for interpretation of ocean color in Case 2 waters.

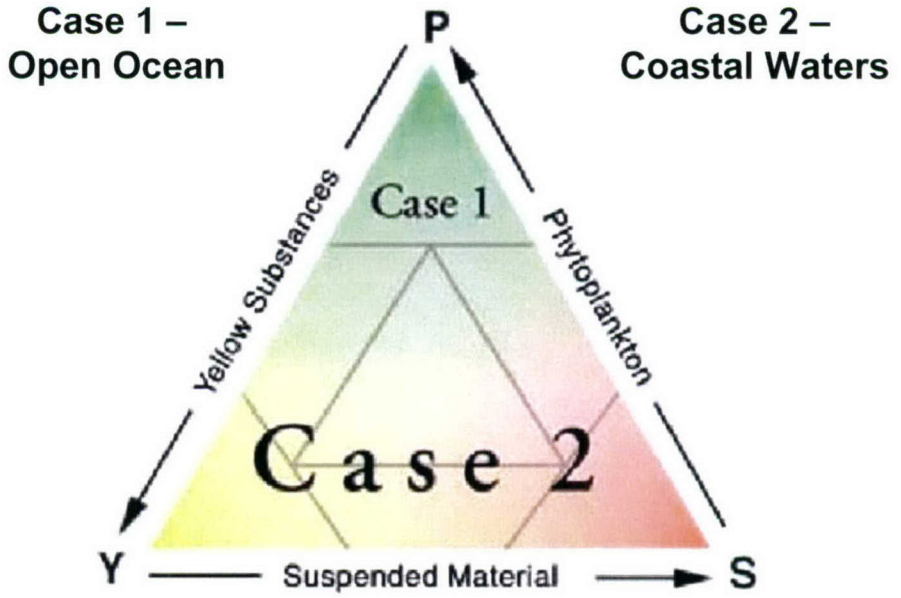

Figure 3-1 Phytoplankton, yellow substances, and suspended material are the three key contributors to the ocean color. Their relative contributions to Case 1 deep ocean and Case 2 coastal waters are depicted.

Looking back on the variety of ocean color sensors for the last 25 years (Figure 3-2), it is noticed that the bands chosen generally vary between 0.4 and 1.0 um. These multispectral sensors vary not only in the number of bands and exact band locations, but also the bandwidths of respective bands. The bands are chosen to utilize the reflection, backscatter, absorption, and fluorescence effects of the various species. While ocean-product algorithms vary based on the parameer and scenario, most of them are semi-empirical retrievals based on established climatological information. As previously mentioned, a challenge to coastal remote sensing is that coastal features are more complex than those of the open ocean. The small number of bands ultimately limits the extent of retrievable products. It would be of great advantage if physics-based approaches could be established as sensors with increasing number in spectral bands provide a chance to solve the complex, coupled phenomena in coastal remote sensing.

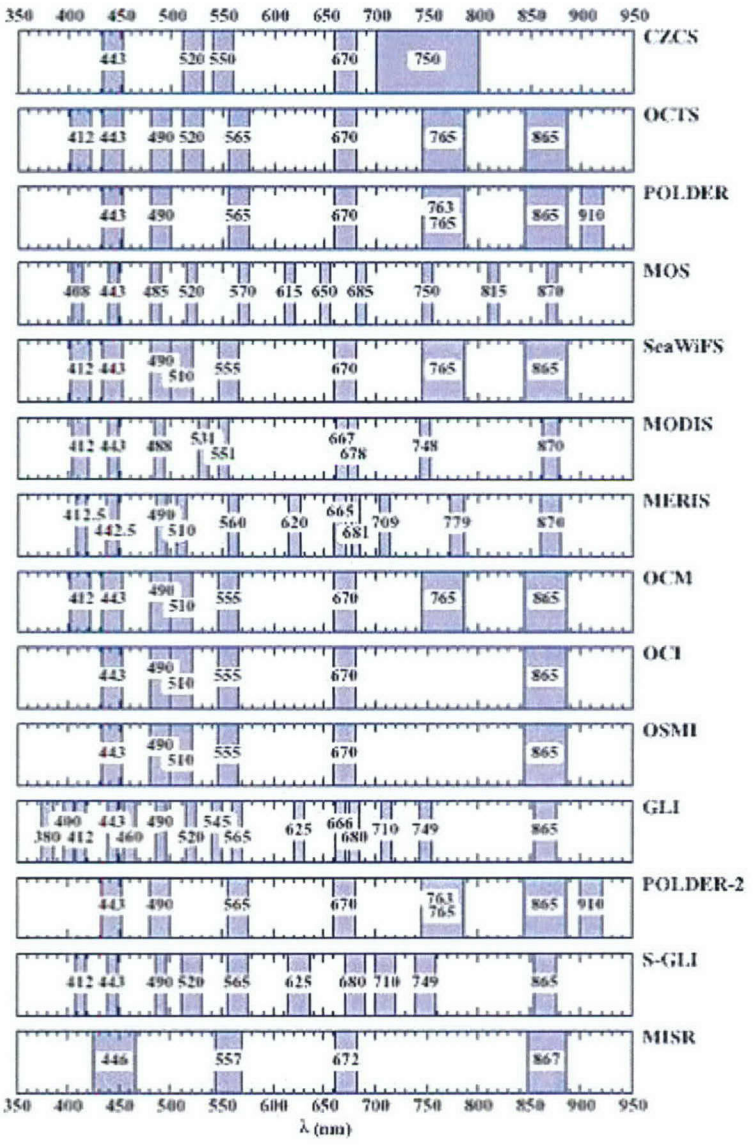

Figure 3-2 Ocean color sensors over the past 25 years.

To illustrate the point, the top of the atmosphere reflectance of ocean can be expressed as (Liew, 2002),

$$R(\lambda) = T_g(\lambda)T_r(\lambda)\ T_a(\lambda)[R_w(\lambda) + R_s(\lambda)] + R_r(\lambda) + R_a(\lambda), \qquad (3\text{-}1)$$

where T_r and T_a are atmospheric transmission factors due to Rayleigh scattering and aerosol scattering, respectively; T_g is the atmospheric gas transmittance, R_w is the water reflectance, R_s is the reflectance of the skylight and direct sunlight from the water surface, and R_r and R_a are the atmospheric path reflectance due to Rayleigh scattering and aerosol scattering, respectively.

Coupled effects can potentially be best resolved with hyperspectral imagery. To begin with, a hyperspectral sensor covering the spectral range between 0.4 and 1 um has all the bands necessary to provide legacy with previous sensors and explore new information. Furthermore, most ocean characterization algorithms utilize water-leaving radiance. The atmospheric aerosol effect is most pronounced in the shortwave visible

where ocean color measurements are made. With contiguous spectral coverage, atmospheric compensation can be done with more accuracy and precision.

3.1 EO-1 Data from Chesapeake Bay

To demonstrate the potential value of Hyperion (and HSI in general) data to coastal characterization, EO-1 data from Chesapeake Bay from 19 February 2002 are analyzed. Both ALI and Hyperion data were available. A common area was selected for analysis. This area is approximately 6 km wide by 15 km long and consists of land, a marsh, a sand bar, and shallow water. Figure 3-3 shows the coastal images of ALI and Hyperion from the data set. Figure 3-4 is the nautical chart from Chesapeake Bay with an enlarged view of the data area. The RGB composite images shown in Fig. 3-3 from ALI and Hyperion look practically identical. For further analysis, spectral data between 430 and 930 nm were utilized: 6 bands from ALI and 50 bands from Hyperion.

To compare the ALI and Hyperion data and to illustrate the dimensionality of data with complex features, the Minimum Noise Fraction (MNF) algorithm is first applied to both ALI and Hyperion data sets. Image reconstruction is then accomplished via the inverse of the transformation matrix. It is compared to the original image to gain insight of the feature space and the extent of the noise in the data. Results are shown in the next section.

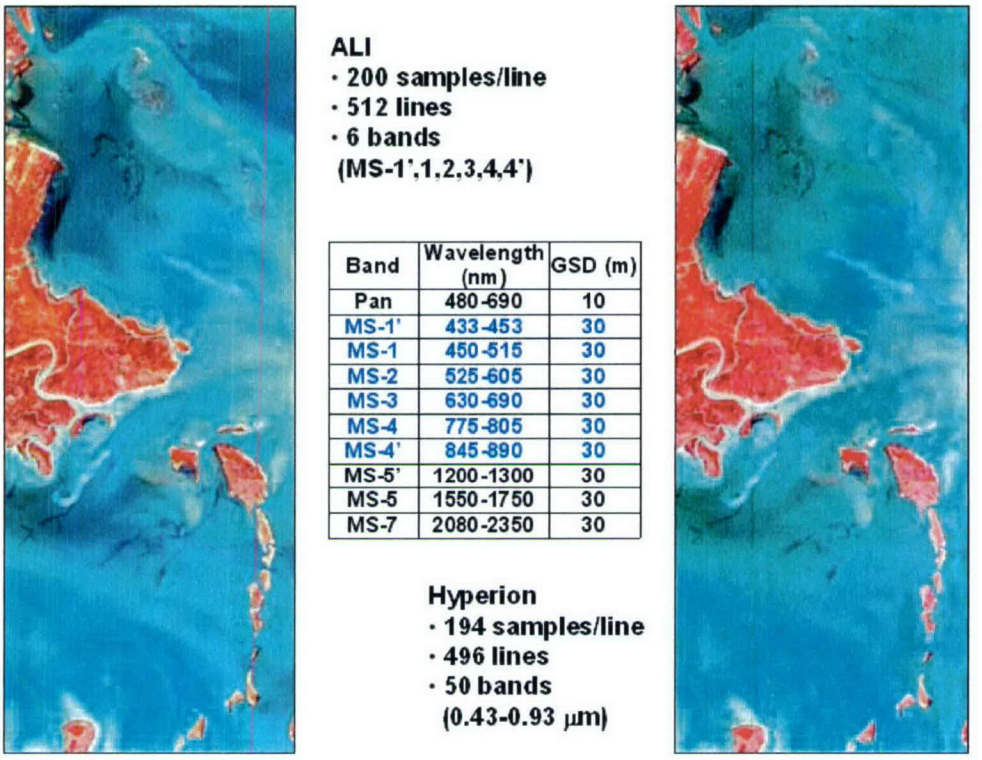

ALI
- **200 samples/line**
- **512 lines**
- **6 bands**
(MS-1',1,2,3,4,4')

Band	Wavelength (nm)	GSD (m)
Pan	480-690	10
MS-1'	433-453	30
MS-1	450-515	30
MS-2	525-605	30
MS-3	630-690	30
MS-4	775-805	30
MS-4'	845-890	30
MS-5'	1200-1300	30
MS-5	1550-1750	30
MS-7	2080-2350	30

Hyperion
- **194 samples/line**
- **496 lines**
- **50 bands**
(0.43-0.93 μm)

Figure 3-3 EO-1 Data from Chesapeake Bay; selected area is ~6 x 15 km^2 in size; spectral bands between 0.43 and 0.93 μm are used for this study.

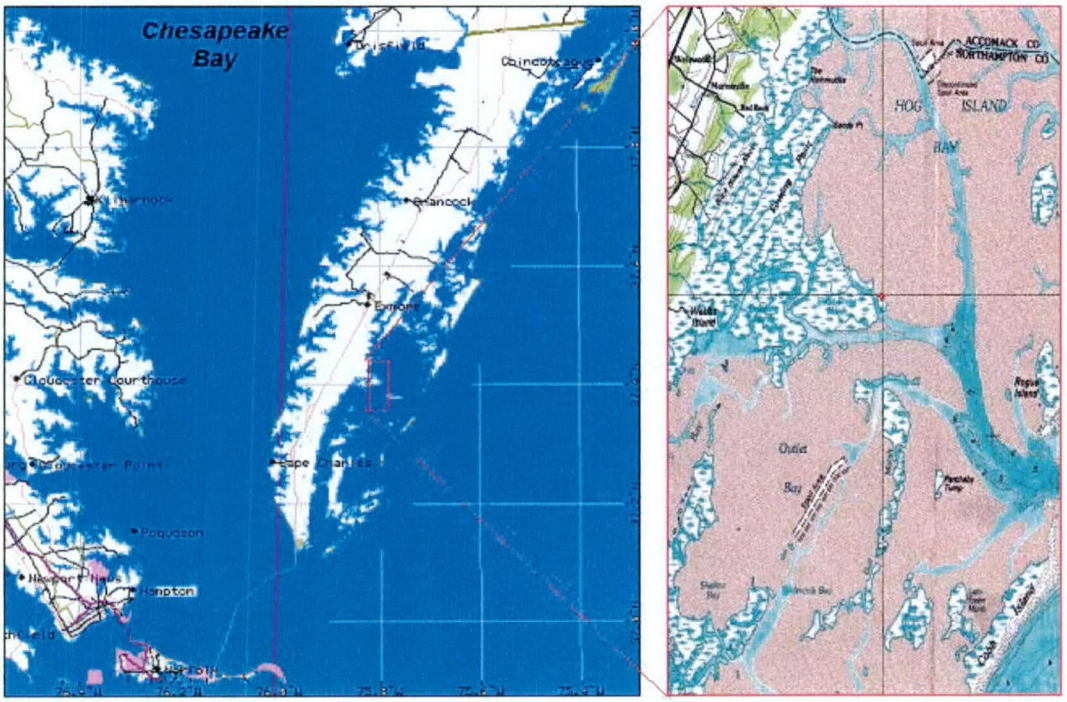

Figure 3-4 Location of EO-1 data from Chesapeake Bay.

3.2 Feature Extraction and Investigation of Information Content

Multispectral and hyperspectral images render themselves amenable to spectral transformations that generate new sets of image components. The transformed image could make evident features not discernible in the original data, or, alternatively, it might be possible to preserve the essential information content of the image with a reduced number of the transformed dimensions.

Principal component analysis uses a linear transformation to translate and rotate multiband data into a new coordinate system that maximizes the variance. This technique is used to de-correlate data and maximize the information content in a reduced number of features (Richards, 1994). The covariance matrix is first computed over the pixel spectra contained in the HSI data cube of interest. Eigenvalues and eigenvectors are then obtained for the covariance matrix Σ as given below:

$$\Sigma = E\left\{(X - X_m)(X - X_m)^T\right\} = \Phi \Lambda \Phi^T, \tag{3-2}$$

where X represents the spectral vector data, X_m the mean spectral vector over the data cube, and E the average operator over the entire data cube. Φ is a matrix consisting of columns of eigenvectors and Λ is a diagonal matrix of eigenvalues.

Using the eigenvectors as a new coordinate system, the HSI data cube is then transformed into principal components, also called eigenimages. These components are ranked in descending order of the eigenvalues (image variances). The eigenimages associated with large eigenvalues contain most of the information while the eigenimages associated with small eigenvalues are noise-dominated. Thus, principal component transform allows for the determination of the inherent dimensionality and segregation of noise components of the HSI data.

The MNF transform is essentially two cascaded principal component transformations (Boardman and Kruse, 1994; Green, et al., 1988). The first transformation, based on an estimated noise covariance matrix, decorrelates and rescales the noise in the data. This first step results in transformed data in which the noise has unit variance and no band-to-band correlations. The second step is a standard principal components transformation of the noise-whitened data. The transformed data can be divided into two parts: one part associated with large eigenvalues and coherent eigenimages, and a complementary part with near-unity eigenvalues and noise-dominated images. The associated eigenvalue of each eigenimage represents the signal-to-noise ratio (SNR). The inherent dimensionality of the data can be determined from the number of coherent eigenimages based on the quantitative SNR. Using the coherent eigenimages, an inverse MNF transformation can be implemented to remove noise from data.

MNF transforms were applied to both ALI and Hyperion data. Results are shown in Figure 3-5. Since only six ALI bands are used, six MNF components are obtained; for Hyperion, there are more MNF components. It is observed that the first few components compare closely with each other. It is noticeable that for the 5th and 6th components, ALI component images are progressively more dominated by noise, while Hyperion

component images suggest more features present. Beyond the 6^{th} component, the 8^{th} and 9^{th} component images, for example, still show discernible features.

It is recognized that the SNR for the Hyperion data is inferior to that for ALI. However, this exercise demonstrated that the increased spectral coverage more than made up for the low SNR and that Hyperion data could be potentially useful for coastal characterization.

Owing to the information compression properties of the principal components transformation, it lends itself to reduced representation of image data with reduced noise. Results of Hyperion image reconstruction are shown in Fig. 3-6. Both 5 and 9 components are used for reconstruction and compared to the original image. As can be seen, the six-component reconstruction clearly shows a sharper image compared to the original, indicating the reduced noise level. However, in comparison to the nine-component reconstruction, it is also evident that there are additional features that were not present in the six-component image that are observed in the nine-component image.

This quick comparative analysis illustrates the potential utility of high dimensionality hyperspectral data as compared to multispectral data even when SNR is less favorable. Also, by transformation of the image data it is possible to enhance the image quality by removing noise components and make features more distinguishable.

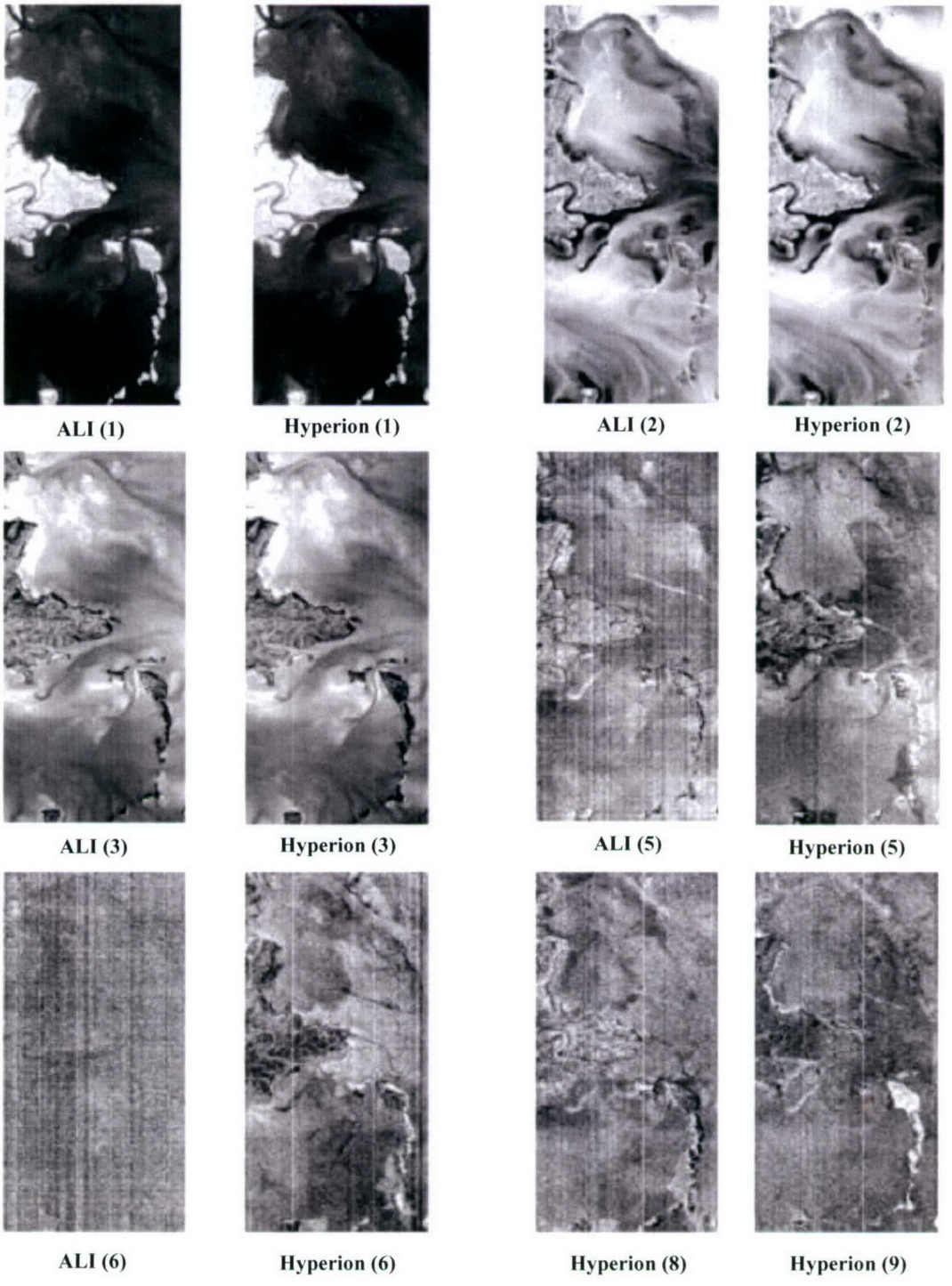

Figure 3-5 Comparison of MNF components from ALI and Hyperion.

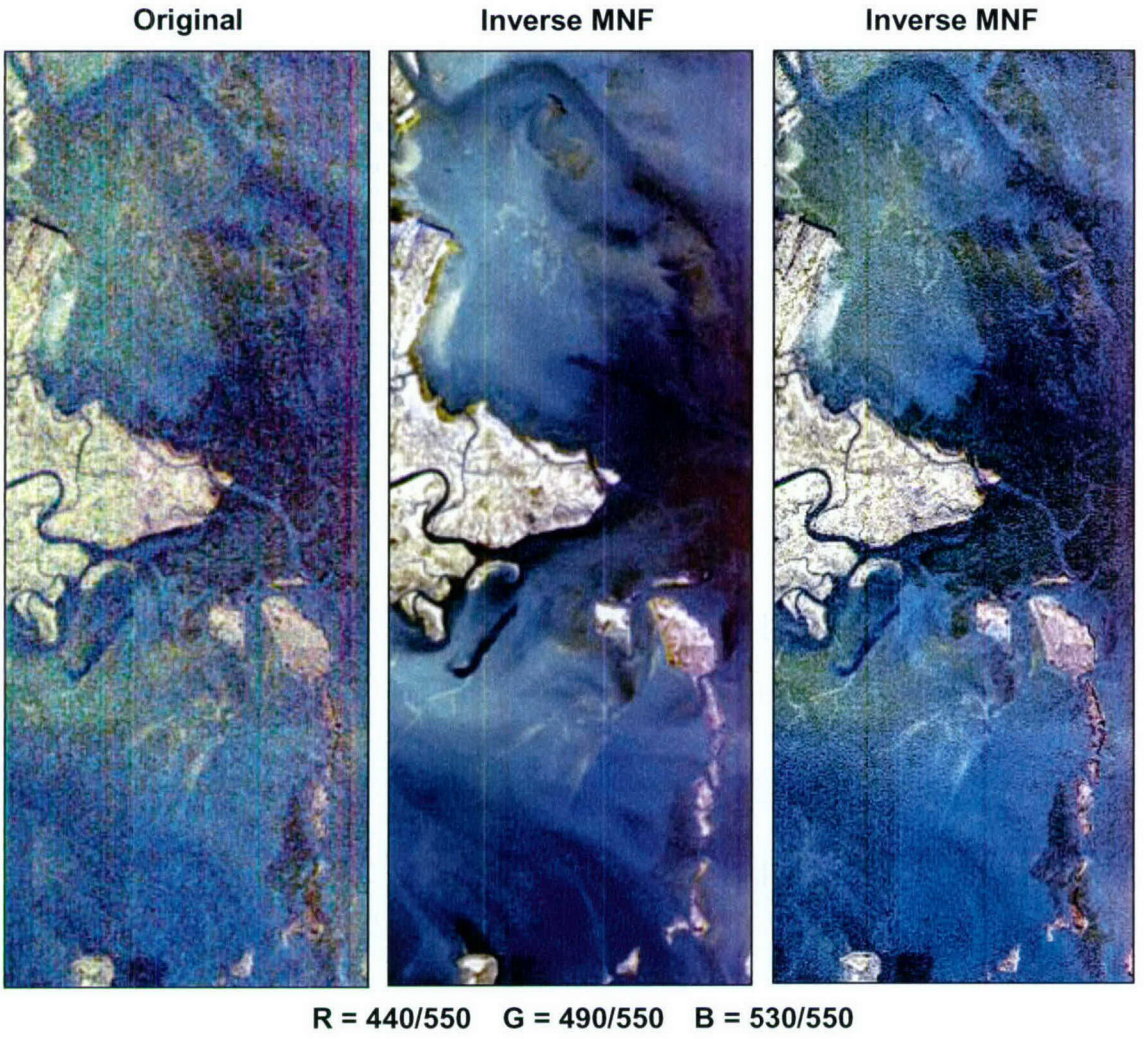

Figure 3-6 Reconstructed images from inverse MNF components and compared to the original image. The false color selection is based on spectral bands commonly used for ocean color characterization.

3.3 Retrieval of Chlorophyll and Comparison with Supporting Data

We will illustrate the retrieval of chlorophyll-a as an example of Hyperion data applications for coastal ocean waters. It is well understood that chlorophyll-a absorbs relatively more blue and red light than green, and the spectrum of backscattered sunlight or color of ocean water progressively shifts from deep blue to green as the concentration of phytoplankton increases. A large data set containing coincident *in situ* chlorophyll and remote sensing reflectance measurements was used to evaluate a wide variety of ocean color chlorophyll algorithms for use by SeaWiFS (O'Reilly, et al., 1998). Two types of algorithms, empirical and semi-analytical, were extensively reviewed. It was concluded that Ocean Chlorophyll (OC)-2 and OC-4 are the two best estimators. Improved performance was obtained with OC-4 algorithm, a four-band (443, 490, 520 and 555 nm), maximum band ratio formulation.

To apply OC-4 to the Chesapeake Bay data, we first use a standard atmospheric correction algorithm to obtain the surface reflectance. The land mass is also masked out. The resultant chlorophyll concentration map is shown in Figure 3-7, with white being the lowest in value. Quantitative values are plotted for selected horizontal lines as well.

Fortuitously, there are supporting data that could be used as "surrogate" ground truth. The first data set came from a routine low-altitude aircraft data collect on 19 February 2002 from the Chesapeake Bay Remote Sensing Program (CBRSP) (see Figure 3-8). The second supporting data set was from the published weekly SeaWifs products for the week of 18–25 February 2002 (see Figure 3-9). All derived values from the various measurements are consistent: in the range from 2 to 4 mg/m^3. Certainly there is much more to do towards validation of the applications of Hyperion data to coastal ocean waters. However, this initial result is very encouraging.

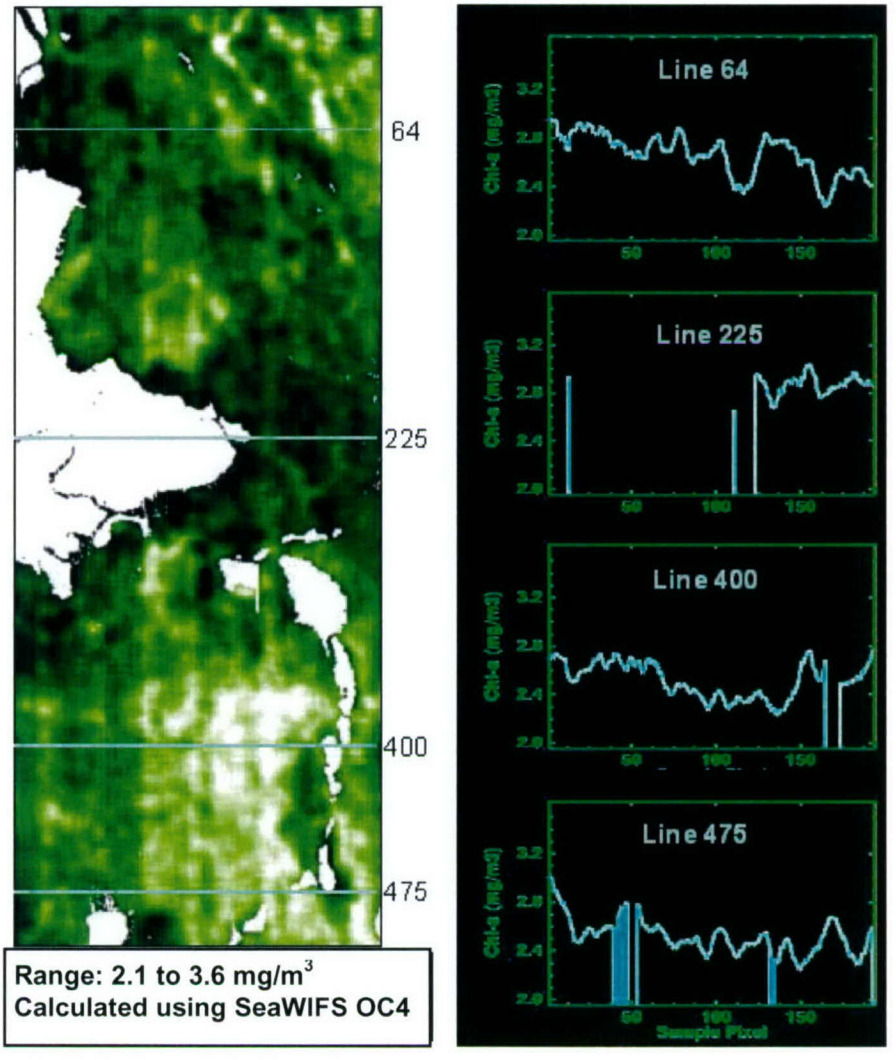

Figure 3-7 Chlorophyll-a retrieval results from SeaWIFS OC4 algorithm.

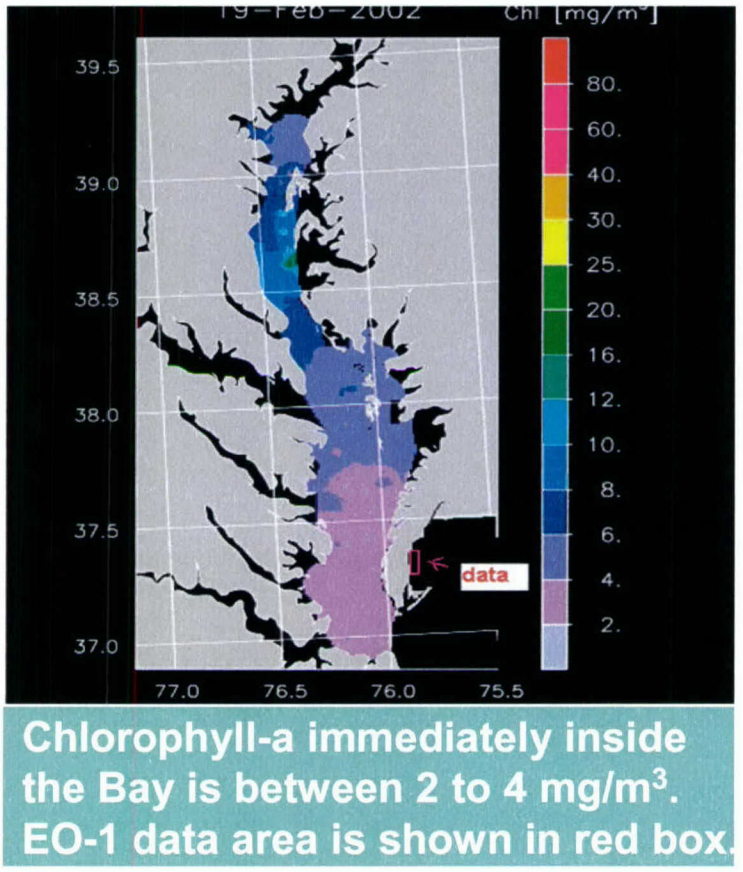

Figure 3-8 Supporting Data from Chesapeake Bay Remote Sensing Program CBRSP. Chlorophyll-a data estimated from a SAS III instrument (SeaWIFS Aircraft Simulator) over well-maintained ground site, and published from the Chesapeake Bay at http://www.cbrsp.org/cbrsp_mainbayintro_page.htm. The aircraft schedule is about twice a month. The flight follows an altitude of 500 ft. The picture in the figure is reproduced from this site (same day as the Hyperion data, 19 February 2002).

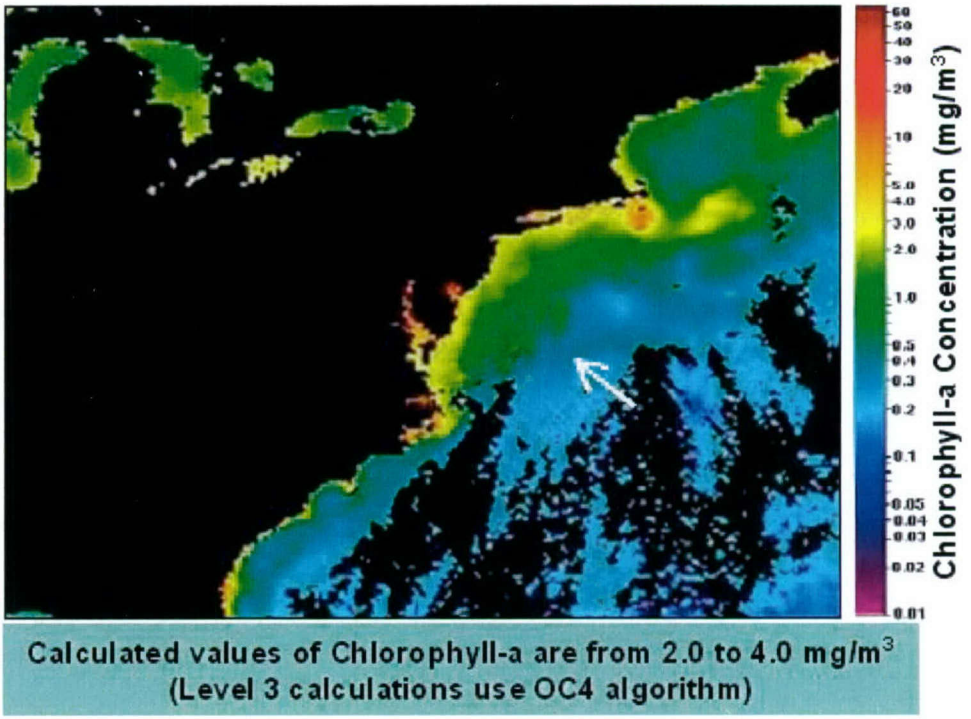

Figure 3-9 SeaWIFS data averaged for the week 2/18/2002 – 2/25/2002. SeaWIFS products published regularly at http://bluefin.gsfc.nasa.gov/cgi/level3.pl. The picture in the figure is for the week 2/18/2002 to 2/25/2002.

3.4 Summary

EO-1 data from Chesapeake Bay from 19 February 2002 are analyzed to demonstrate the potential value of Hyperion (and HSI in general) data to coastal characterization. It is first illustrated that hyperspectral data inherently provide more information for feature extraction than multispectral data although Hyperion has lower SNR than ALI. Chlorophyll retrievals are also shown. The results compare favorably with data from other sources. Future measurement requirements (airborne and space-borne) are also discussed.

4. TERRESTRIAL ANALYSIS APPLICATIONS

To demonstrate the utility of EO-1 data, combined analysis of panchromatic, multispectral (ALI, Advanced Land Imager), and hyperspectral (Hyperion) data was conducted. In particular, the value added by HSI with additional spectral information will be illustrated (Hsu, et al., 2003).

As described earlier, Hyperion is a pushbroom-imaging spectrometer. Each square pixel subtends 30 m, sampled every 30 m and measures a complete spectrum from 400 to 2500 nm in 220 spectral channels. Each image covers a ground area of 7.65 km x 185 km. Advanced Land Imager (ALI) is a co-incident multispectral imaging (MSI) sensor also on board EO-1. ALI (see Table 4-1) covers a larger area (37-km swath width) with the same spatial resolution but in nine broad bands. The area covered by ALI overlaps approximately 80% with that of Hyperion. In addition, it has a high-resolution panchromatic band of 10-m pixel resolution, which is three times better than that of the ALI MSI and Hyperion HSI. The purpose of this section is to demonstrate the utility of EO-1 data with combined analysis of panchromatic, multispectral (ALI) and hyperspectral (Hyperion) data.

Table 4-1 ALI Spectral Bands and Spatial Resolutions

Band	Wavelength (μm)	GSD (m)
Pan	0.48-0.69	10
MS-1′	0.43-0.45	30
MS-1	0.45-0.52	30
MS-2	0.53-0.61	30
MS-3	0.63-0.69	30
MS-4	0.78-0.81	30
MS-4′	0.85-0.89	30
MS-5′	1.20-1.30	30
MS-5	1.55-1.75	30
MS-7	2.08-2.35	30

Data sets from Coleambally Irrigation Area, Australia, on 7 March 2000 and the San Francisco Bay area on 17 January 2000 are analyzed. Atmospheric correction is first applied to radiance data (used ATREM by Gao, et al., 1996). Hyperion and ALI data over Coleambally Irrigation Area, Australia, are used for terrain characterization in terms of soil moisture content and vegetation status. Hyperion data are also subject to spectral unmixing to illustrate sub-pixel analysis. Abundance levels of lush vegetation and bare soil are estimated for image pixels in different fields of crops. Anomaly detection algorithms are applied to Hyperion data over the San Francisco Bay area. Detections

from Hyperion data are compared with previous AVIRIS data and known library spectra for material identification. In addition, pan-sharpened ALI is also shown for enhanced visualization of spatial features.

4.1 Terrain Characterization

Vegetation status and soil moisture content are two major factors determining terrain trafficability. As an example, EO-1 data from Coleambally Irrigation Area, consisting both of bare soil and various types of vegetation, are used to illustrate applications of terrain characterization. Simultaneous multispectral and hyperspectral data are also compared.

In the vegetation spectra shown in Figure 4-1, we observe a decrease in the radiance at 0.68 μm and a large increase at near infrared since chlorophyll in the vegetation absorbs visible light from the sun and reflects the infrared radiation. The Normalized Difference Vegetation Index (NDVI) measuring spectral differences around the red edge is commonly used to represent the health and amount of vegetation.

$$NDVI = \frac{\rho(0.86\mu m) - \rho(0.66\mu m)}{\rho(0.86\mu m) + \rho(0.66\mu m)} \tag{4-1}$$

where, ρ(0.66 μm) and ρ(0.86 μm) are reflectance at 0.66 μm and 0.86 μm, representing red and near-infrared band reflectance, respectively.

Under smoky or cloudy conditions, both obscurants tend to mask the underlying signal at visible and near IR wavelengths (Griffin, et al., 2000). However, information identifying vegetation can be retrieved from spectral channels at longer wavelengths, which are transmitted through some smoke. The Liquid Water Index (LWI) estimates water content based on reflectance differences between 1.1 μm and 2.2 μm.

$$LWI = \frac{\rho(1.1\mu m) - \rho(2.2\mu m)}{\rho(1.1\mu m) + \rho(2.2\mu m)} \tag{4-2}$$

A comparison of the spectral characteristics of the channels used in the LWI (1.1μm and 2.2 μm) and those used for the NDVI (0.64 μm and 0.86 μm) shows a similar but reversed trend between dense and sparse or no vegetation conditions (see Figure 4-1). While NDVI captures the state of vegetation via chlorophyll content, LWI is indicative of the liquid water content in the vegetation. Therefore, it is not surprising that LWI, like NDVI, has the capability to discriminate between vegetation conditions, but with the added benefit of operating under obscured conditions.

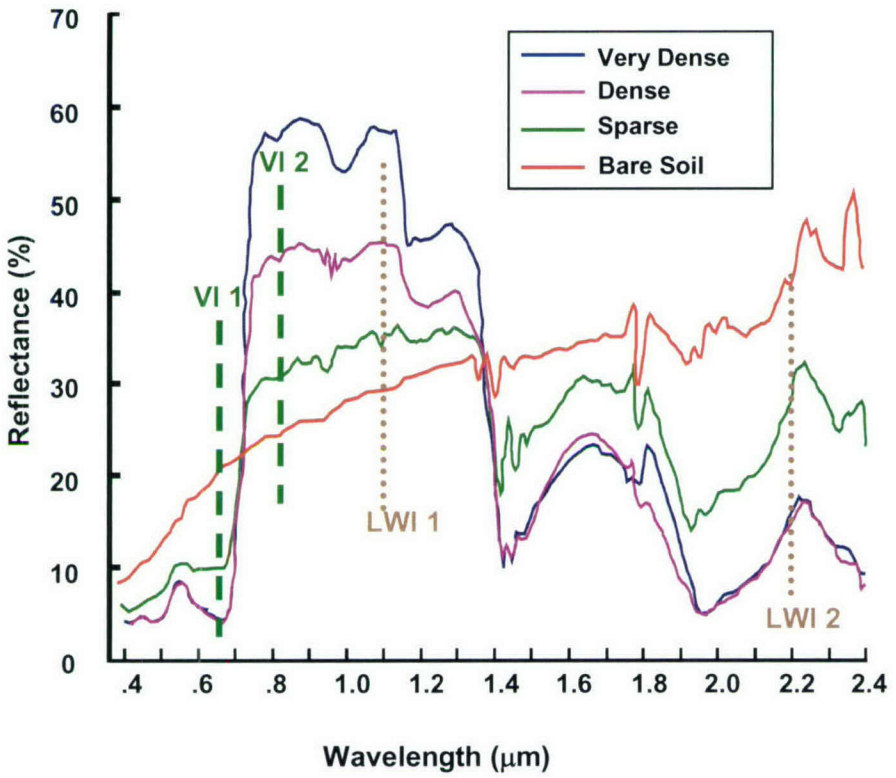

Figure 4-1 Sample vegetation and soil spectra. The Normalized Difference Vegetation Index (NDVI) measuring spectral differences around the red edge is commonly used to represent the health and amount of vegetation. The Liquid Water Index (LWI) estimates water content based on reflectance differences between 1.1 μm and 2.2 μm.

Another index based on Landsat 7 ETM+ bands 5 and 7 is the Soil Moisture Index (SMI) (Musick and Pelletier, 1986).

$$SMI = \frac{\rho(1.55 - 1.75\mu m)}{\rho(2.08 - 2.35\mu m)} \tag{4-3}$$

These indices are calculated for the Coleambally image using both Hyperion and ALI data. ALI bands closest to the wavelengths indicated in the index formulae are used. Bands MS-3 and MS-4′ are employed for NDVI and MS-5′, and MS-7 for LWI. For comparison, Hyperion spectral data are averaged over the bandwidth of corresponding ALI bands before index calculation. Figure 4-2 shows line profiles of NDVI, LWI and SMI over areas of soil, corn, rice, and soybean in the image. The LWI profile appears to closely follow the NDVI profile, except for some small deviations. The SMI profile also resembles the NDVI profile in overall shape but has a different scale since it is calculated as a band ratio rather than as a normalized band difference like the NDVI and LWI. The indices are high at the soybean area, indicating most lush condition, and low at the two soil areas for little or no vegetation. Comparing the profiles derived from Hyperion and ALI data, the two sets are nearly identical although some noise is apparent from pixel to pixel in the profiles derived from Hyperion data.

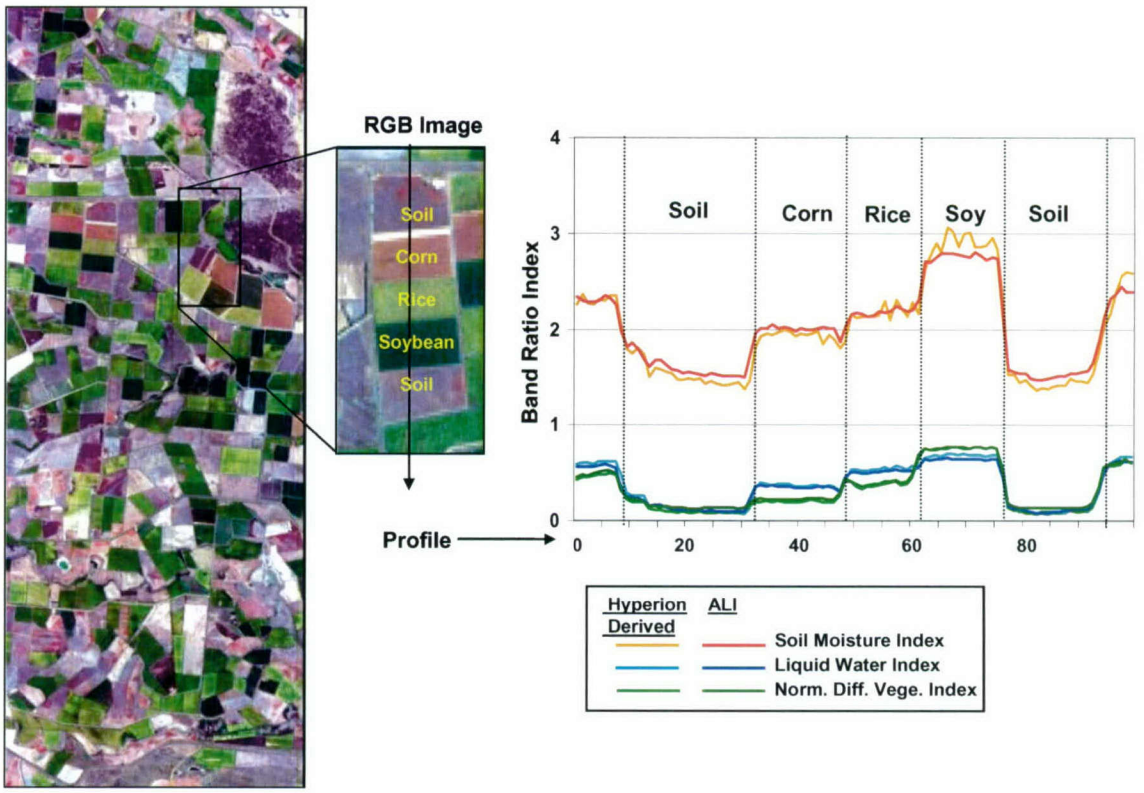

Figure 4-2 Line profiles of NDVI, LWI, and SMI over areas of soil, corn, rice, soybean, and a second plot of soil. The LWI profile appears to closely follow the NDVI profile, except for some small deviations. The SMI profile also resembles the NDVI profile in overall shape but has a different scale.

To further examine the correlations between LWI and NDVI, we plot the indices derived from Coleambally Hyperion data in a scatter plot (see Figure 4-3). Separate clusters can be delineated from the index plot due to various LWI-NDVI correlations of different material. The cluster located at lower left—low LWI and NDVI less than 0.2—consists of data from soil. In this region, there is little change in NDVI. Some spread in the LWI dimension is seen, indicating different levels of moisture content in the soil. The cluster in the middle extends LWI values from approximately 0.15 to 0.45 and NDVI from 0.2 to 0.5. This cluster results from pixel data with mixtures of soil and vegetation. The cluster at the top represents data from vegetation and has a larger extent in NDVI than in LWI. This indicates that LWI, while strongly correlated with NDVI, is less sensitive to vegetative state than the vegetation index. Reexamination of Figure 4-2 in this light reinforces this conclusion, as deviations from 0.5 in the index are more exaggerated by NDVI than by the LWI.

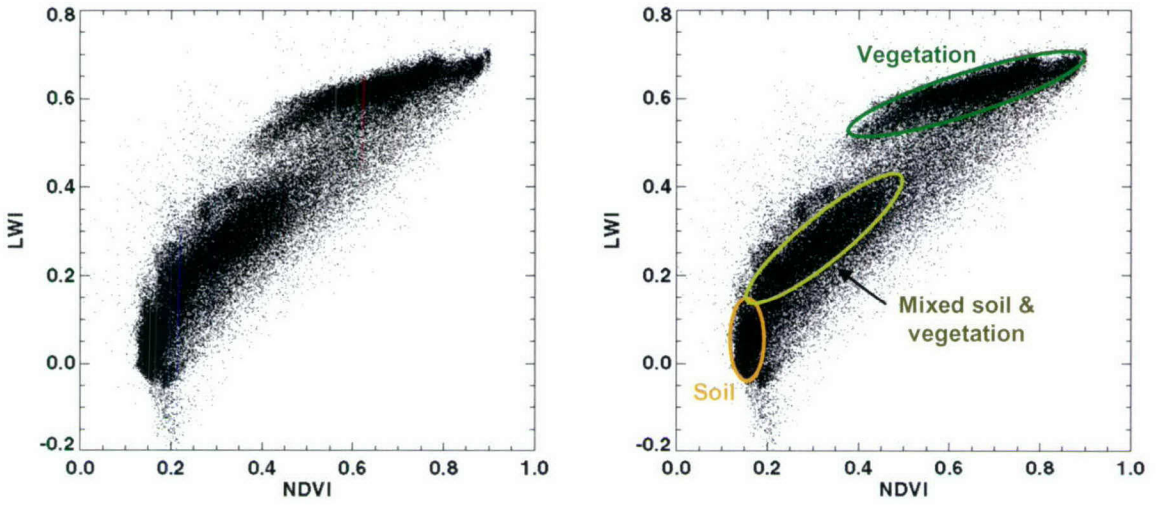

Figure 4-3 Scatter plot of LWI and NDVI derived from Hyperion data over Coleambally. Separate clusters can be delineated from the index plot as shown on the right. The cluster located at lower left consists of data from soil. Some spread in the LWI dimension is seen, indicating different levels of moisture content in the soil. The cluster at the top represents data from vegetation and has a larger response in NDVI than in LWI.

The soil and vegetation clusters are further divided into smaller regions to observe the progressive change in spectral characteristics. As shown in Figure 4-4, the regions colored in orange, light sienna, and dark sienna represent soil while five shades from yellow to dark green delineate vegetation conditions. Image pixels contributing to the various regions defined in the scatter plot in Figure 4-4 are mapped with the corresponding colors as shown on the right in Figure 4-4. Most mapped fields are mono- or dichromatic, representing certain soil or vegetation status, not a random mixture of several colors. This indicates these fields are relatively uniform. The areas not mapped are mostly mixtures of soil and vegetation. The mean spectra of different regions are plotted in Figure 4-5. The soil with less moisture has a higher reflectance in SWIR (1–2.5 μm). In the vegetation spectra, the different changes of reflectance between 0.64 μm and 0.86 μm agree well with the NDVI values defined for the regions. Dividing the entire LWI-NDVI space (scatter plot at left of Figure 4-4) allows for characterization of the fields. As illustrated in the case of Coleambally Irrigation Area, different fields are characterized with the moisture content and vegetation status.

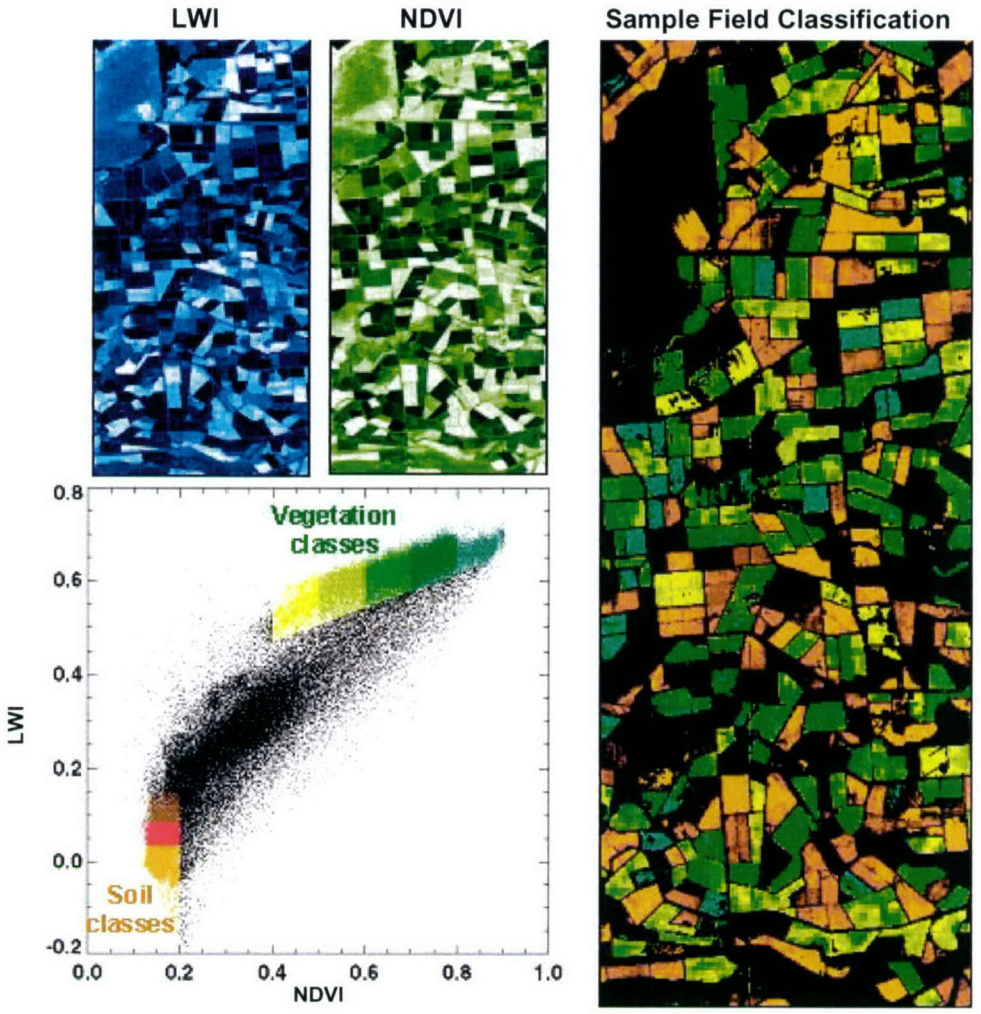

Figure 4-4 Soil and vegetation clusters in the scatter plot on the left are divided in eight regions. Regions colored in orange, light sienna, and dark sienna represent soil while five shades from yellow to dark green delineate vegetation. Image pixels contributing to the various regions defined in the scatter plot are mapped with the corresponding colors on the right. The areas not mapped are mostly mixtures of soil and vegetation.

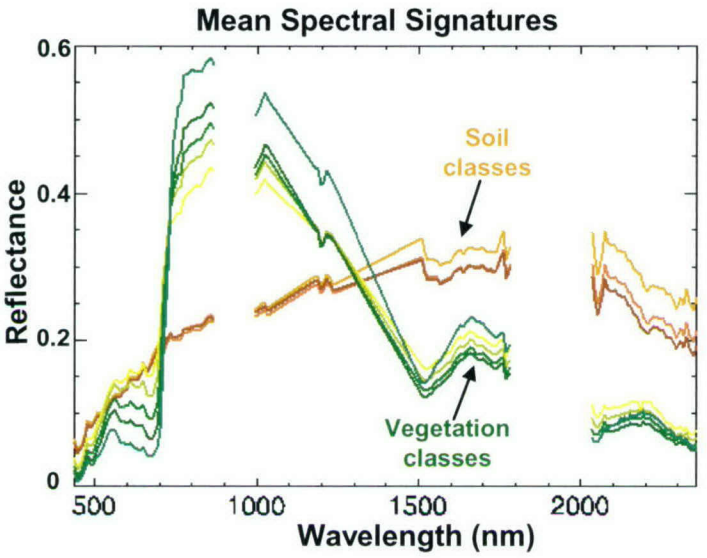

Figure 4-5 Mean spectra of soil and vegetation regions. The soils with less moisture content have higher reflectance in SWIR (1–2.5 μm). In the vegetation spectra, the different changes of reflectance between 0.64 μm and 0.86 μm agree well with the NDVI values defined for the regions.

4.2 Spectral Unmixing

The pixel resolution of both Hyperion HSI and ALI MSI is 30 m on the ground. If there are different types of material in the pixel, each contributes to the combined spectral measurement. Assuming linear combination of M types of material and each material occupies a_m fraction of the pixel, the pixel spectrum, ρ_T can be written as below:

$$\rho_T = \sum_{m=1}^{M} a_m \rho_m \tag{4-4}$$

where $m = 1...M$, representing the material type; $0 \le a_m \le 1$, $\Sigma a_m = 1$, a_m is a different fraction of each material m within the pixel.

Given the contributing materials, the material abundance in a pixel can be recovered from HSI data with various least-squared-error unmixing algorithms (Keshava and Mustard, 2002). An unmixing algorithm is unconstrained when the fractions are not limited to the conditions of $0 \le a_m \le 1$ and $\Sigma a_m = 1$.

Figure 4-6 shows sample areas of soybean and soil in the Coleambally image. Regions of interest are selected as shown on the Hyperion image to include a lush vegetative area in the soybean field and a bare region in the soil area. The mean spectra of the regions are used to demonstrate a two-class unmixing analysis of lush vegetation and bare soil. The unconstrained least-squares unmixing algorithm is applied to the image. The retrieved soybean and soil abundances are shown at the left side of Figure 4-7.

Abundance values of pixels at the horizontal line indicated in the abundance images are plotted at the right side of Figure 4-7. Results show 100% soybean for samples 15 to 20, mixtures of soybean and soil for samples 21 to 34, and 100% soil for samples 35 to 42. The abundance of soybean decreases progressively from left to right while soil increases in the mixture at the transitional region. Sample number 28 appears near the middle of the transition. The abundance retrieval quantifies the amount of soybean and bare soil in the transitional region. This illustrates how an unmixing algorithm can be applied to HSI data to obtain quantitative information of different materials in a given pixel.

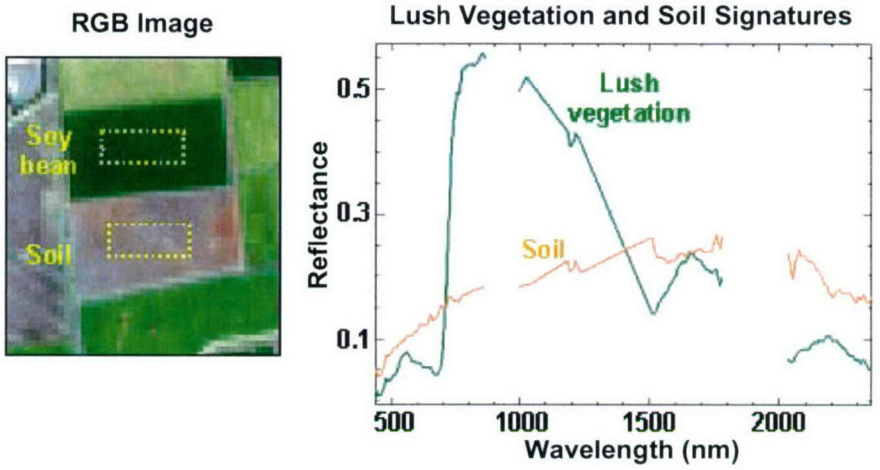

Figure 4-6 Sample areas of soybean and soil in the Coleambally image. Regions of interest are selected as shown on the Hyperion image to include a lush vegetative area in the soybean field and a bare region in the soil area. The mean spectra of the regions are used to demonstrate a two-class unmixing analysis of lush vegetation and bare soil.

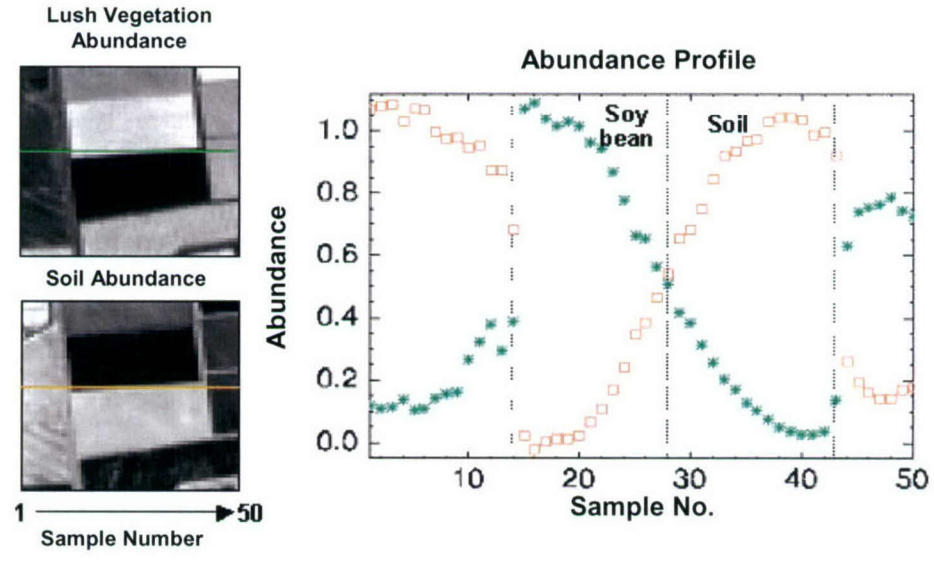

Figure 4-7 Retrieved soybean and soil abundances from the Hyperion data. The plot at right shows abundances for pixels at the horizontal line of the image. The abundance of soybean decreases progressively from left to right while soil increases in the mixture at the transitional region. Sample number 28 appears near the middle of the transition.

4.3 Spectral Feature Analysis

Hyperion data were collected over San Francisco Bay on 17 January 2000. There have been several AVIRIS collects over the same area. One of the earlier AVIRIS collects, from 20 June 1997, is used here for comparison with Hyperion. Some common features, such as water, runway, and grass, are selected for comparison. ATREM (Gao, et al., 1996) was first applied to both data sets for atmospheric compensation so that both data sets are reduced to spectral reflectance values. As shown in Figure 4-8, spectral features from both data sets appear very similar except that Hyperion data are lower in all reflectance values.

The Minimum Noise Fraction (MNF) transformation (Green, et al., 1988) algorithm is then applied for further feature extraction. Clusters of anomalous pixels are detected in the 10^{th} component. Analysis of the AVIRIS data also found anomalies detected at the same location as in the Hyperion data. The common detection is shown in Figure 4-9. The sharpened ALI image with the high-resolution panchromatic band included in the figure shows similar spatial features as the AVIRIS image at the detection. (Note: AVIRIS spatial resolution is 20 m.) Spectral signatures of the detections from both Hyperion and AVIRIS data are plotted in Figure 4-10.

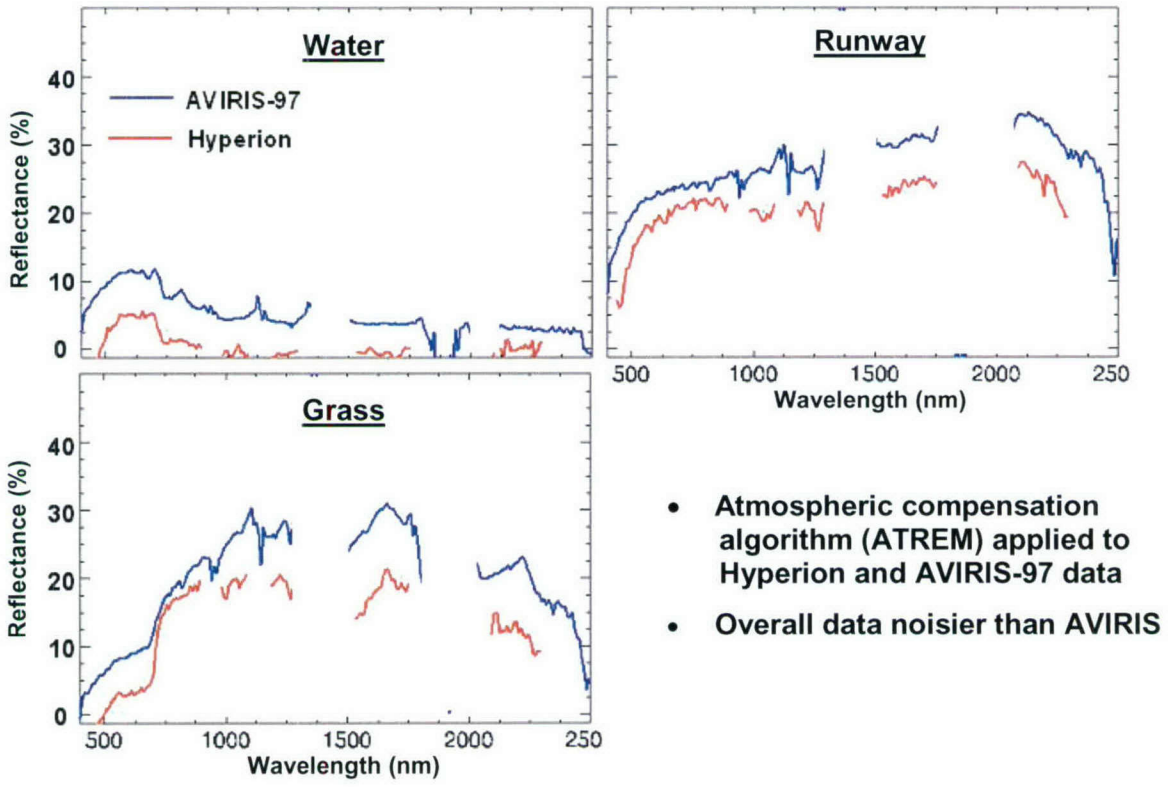

Figure 4-8 Hyperion and AVIRIS data on selected features. Hyperion and AVIRIS data appear similar in overall spectral shapes, except that the Hyperion data are consistently lower in their reflectance signatures.

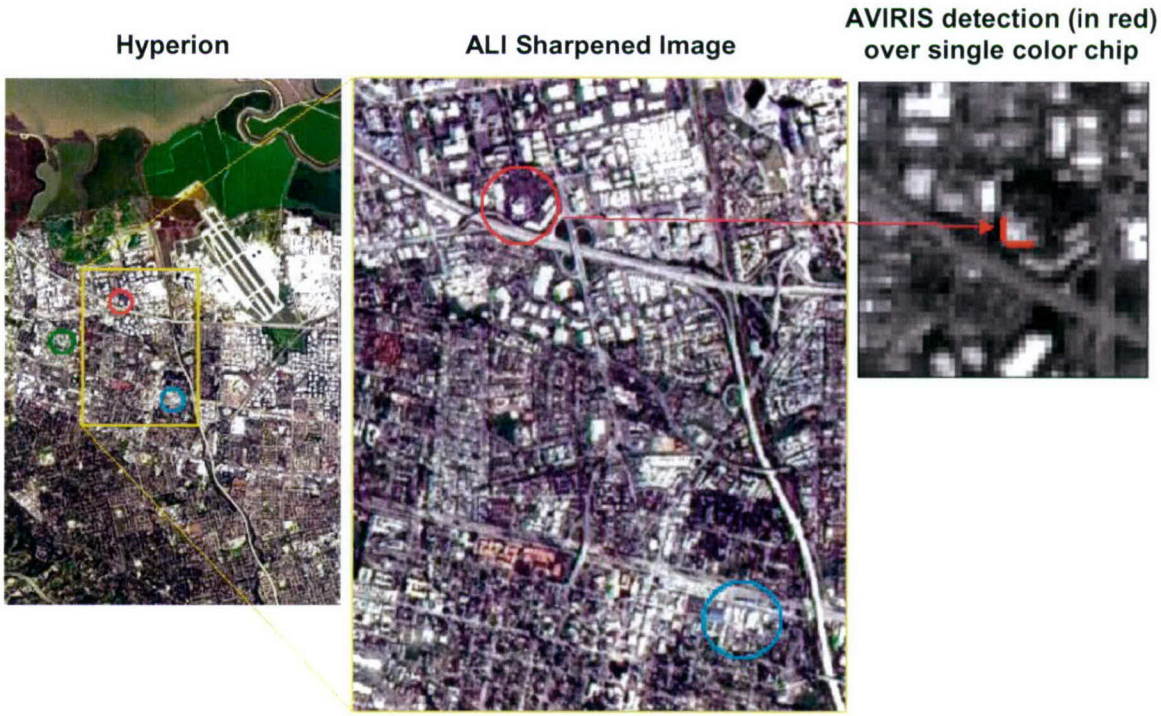

Figure 4-9 Anomaly detections in Hyperion and AVIRIS data. The sharpened ALI image with the high-resolution panchromatic band included on the right shows similar spatial features as the AVIRIS image at the detection.

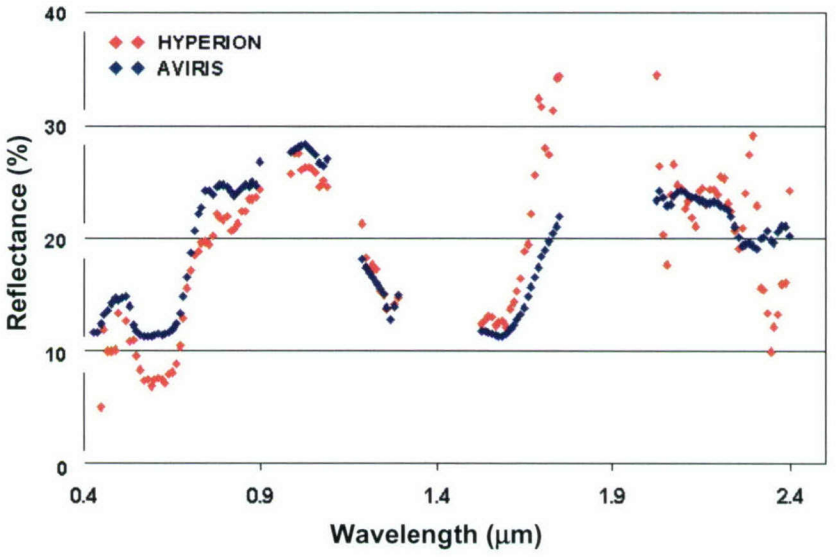

Figure 4-10 Spectral signatures of anomaly detections from Hyperion and AVIRIS data. The detections appear similar in spectral shapes to a type of paint in our spectral library.

A photograph of the building at the detected site was obtained (see Figure 4-11). The detections in the HSI data appear to be of the blue roofs of the building. For verification, sample panels of material similar to the roofs were acquired and measured with a handheld spectrometer. The spectral signatures of the roof panels are plotted together with the detected data from both Hyperion and AVIRIS images in Figure 4-12. The Spectral Angle Mapper (SAM) algorithm is also applied to the panel signatures with reference to the AVIRIS signature. The resulting spectral angles vary from 0.162 to 0.307 radians (9.3^{o} to 17.6^{o}). The signatures compare well in overall shape, with a smaller vertical offset than is apparent in Figure 4-8.

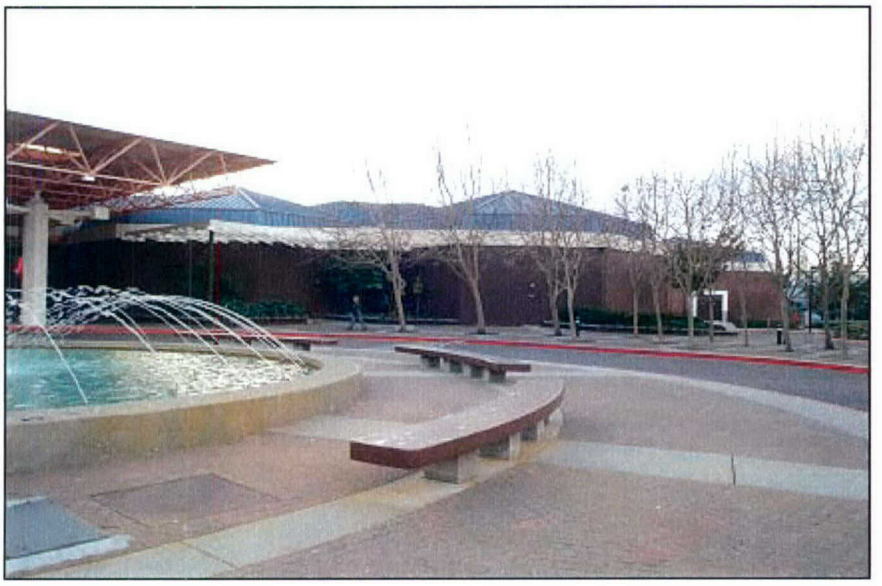

Figure 4-11 Photo of building at the detected site. The detections in the HSI data appear to be of the blue roofs of the building.

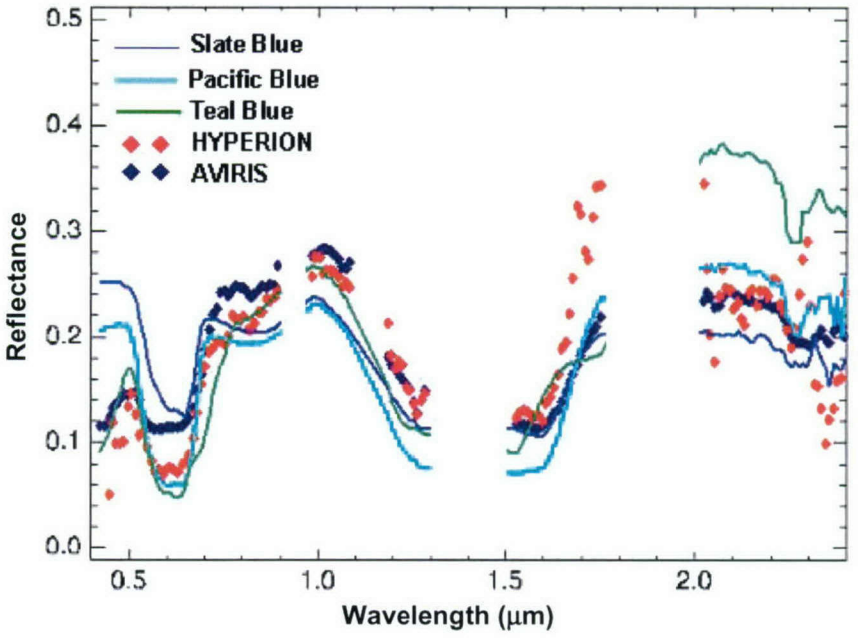

Figure 4-12 Spectral signatures of the roof panels plotted together with the detected data from Hyperion and AVIRIS images. The signatures compare well in overall shape, but are somewhat different in details.

4.4 Terrestrial Analysis Summary

Examples of EO-1 Hyperion data applications are shown for terrain characterization, spectral unmixing, and anomaly detection. Data used include those from Coleambally Irrigation Area, Australia, (7 March 2000) and San Francisco Bay area (17 January 2000). For terrain characterization, it is illustrated that various simple indices can be used to characterize the soil and vegetation conditions. They include the Normalized Difference Vegetation Index (NDVI), the Liquid Water Index (LWI) and the Soil Moisture Index (SMI). Consistent results were demonstrated between Hyperion and ALI. These indices were further used to map the bare and vegetated fields with promising results. For spectral unmixing, some adjacent fields with distinctly different materials (soil and verdant soybean) were used for sub-pixel analysis. The results illustrate how unmixing algorithms can be applied to HSI data to obtain quantitative abundance information of the materials contained in a given pixel.

The Hyperion data from San Francisco Bay area were used first to compare with AVIRIS data collected some two-and-a-half years earlier. Anomaly detection algorithms were then applied to both data sets. A building complex with distinct roof material was detected using both images. Subsequently, samples of similar roof panels were acquired and their spectral signatures measured with a handheld spectrometer, thus corroborating the detections by Hyperion and AVIRIS.

5. SUMMARY

Three examples demonstrating utilities of the EO-1 sensor data in different applications are described in this report: cloud-cover analysis, coastal-water feature extraction, and terrestrial analysis applications.

Cloud-cover analysis deals primarily with the problem of discrimination of clouds from surface features. A simplified cloud-detection algorithm was developed that utilizes only six bands in reflected solar measurements from the EO-1 Hyperion sensor to discriminate clouds from all other features in the image. The selection of the six bands provided spectral information at critical wavelengths while keeping processing costs to a minimum since both onboard computer memory and processing time are limited for this intended application. The cloud-cover detection process was applied to a set of 20 Hyperion scenes with varying cloud cover and type, surface characteristics, and seasonal collection times.

Coastal-water feature extraction analysis was performed on EO-1 data over Chesapeake Bay on 19 February 2002 to demonstrate the potential value of Hyperion data to coastal characterization. Spectral applications for ocean waters were briefly discussed. EO-1 data from both multispectral (ALI) and hyperspectral (Hyperion) sensors were compared to establish the relative quality and additional feature-extraction potential for Hyperion data. Chlorophyll retrieval was carried out using an existing simple algorithm. The results compared favorably with data from other satellite and aircraft sources.

For the additional utility of EO-1 data, application examples are shown for terrain characterization, spectral unmixing and anomaly detection. Data sets from Coleambally Irrigation Area, Australia, on 7 March 2000 and the San Francisco Bay area on 17 January 2000 were employed for the analysis. Soil and vegetation properties, such as soil moisture, vegetation chlorophyll, and plant liquid water, were explored to characterize various agriculture fields. Spectral unmixing, feature extraction, and anomaly detection algorithms were also applied for different applications.

In each of the applications considered, it is shown that hyperspectral data provide utility; in some cases only a few selected bands were used, while in other applications full spectral information is explored. The ultimate strength of hyperspectral remote sensing is exactly its versatility in data use: simple band thresholds, ratios, and differences are used to take advantage of known phenomenology. Signal processing approaches, such as anomaly detection and matched-filtering algorithms, take advantage of the full spectral data such that subtle differences can be explored. This report explores both approaches and a variety of applications are illustrated.

ACRONYMS

AC	Atmospheric Compensation
ALI	Advanced Land Imager
ATREM	ATmosphere REMoval program
AU	Astronomical Units
AVHRR	Advanced Very-High-Resolution Radiometer
AVIRIS	Airborne Visible-InfraRed Imaging Spectrometer
BI	Burn Index
DEM	Digital Elevation Model
GOES	Geostationary Operational Environmental Satellite
HSI	HyperSpectral Imagery
HTAP	Hyperspectral Technology Assessment Program
JPL	Jet Propulsion Laboratory
K	Kelvin
LWI	Liquid Water Index
MNF	Minimum Noise Fraction
MSI	MultiSpectral Imagery
MODTRAN	MODerate resolution TRANsmission model
MSL	Mean Sea Level
NDVI	Normalized Difference Vegetation Index
NIR	Near InfraRed
NOAA	National Oceanic and Atmospheric Administration
PC	Principal Component
PCA	Principal Component Analysis
RGB	Red Green Blue
SAM	Spectral Angle Mapper
SCAR-B	Smoke, Cloud, Aerosol and Radiation Experiment – Brazil
SMI	Soil Moisture Index
SNR	Signal-to-Noise Ratio
SWIR	Shortwave InfraRed
UTC	Universal Time Coordinated
VIS	Visible
WNW	West North West
µflicks	Radiation Units of $\mu W\ cm^{-2}\ sr^{-1}\ \mu m^{-1}$

REFERENCES

Ackerman, S.A., K.I. Strabala, W.P. Menzel, R.A. Frey, C.C. Moeller, and L.E. Gumley, "Discriminating clear sky from clouds with MODIS," *J. Geophy. Res.*, **103**, pp. 32141–32157, 1998.

Berk, A, L.S. Bernstein, G.P. Anderson, P.K. Acharya, D.C. Robertson, J.H. Chetwynd, and S.M. Adler-Golden, "MODTRAN Cloud and Multiple Scattering Upgrades with Application to AVIRIS," *Remote Sens. Environ.*, **65**, pp. 367–375, 1998.

Boardman, J.W., and F.A. Kruse, "Automated spectral analysis: a geological example using AVIRIS data, north Grapevine Mountains, Nevada," *Proceedings, ERIM Tenth Thematic Conference on Geologic Remote Sensing*, Environmental Research Institute of Michigan, Ann Arbor, MI, pp. I407–I418, 1994.

Burke, H.K., B. Misra, S. Hsu, M. Griffin, C. Upham, and K. Farrar, "EO-1 Analysis Applicable to Coastal Characterization," in Proceedings of SPIE Vol. 5093 *Algorithms and Technologies for Multispectral, Hyperspectral, and Ultraspectral Imagery IX*, edited by Sylvia S. Shen, Paul Lewis, (SPIE, Bellingham, WA, 2003) pp. 507–516.

Gao, B-C and Y.J. Kaufman, "Correction of Thin Cirrus Effects in AVIRIS Images Using the Sensitive 1.375-μm Cirrus Detecting Channel," *Summaries of the Fifth Annual JPL Earth Science Workshop*, JPL Publication 95-4, pp. 59–62, Pasadena CA, 1995.

Gao, B.-C., K.B. Heiderbrecht, and A.F.H. Goetz; "Atmosphere Removal Program (ATREM) Version 2.0 Users Guide," Center for the Study of Earth from Space/CIRES, University of Colorado, Boulder, CO, 1996.

Gao, B.-C, Y.J. Kaufman, W. Han, and W.J. Wiscombe, "Removal of Thin Cirrus Path Radiances in the 0.4 – 1.0-μm Spectral Region Using the 1.375-μm Strong Water Vapor Absorption Channel," *Summaries of the Seventh JPL Airborne Earth Science Workshop*, JPL Publication 97-21, pp. 121–130, Pasadena CA, 1998.

Green, A. A., M. Berman, P. Switzer, and M.D. Craig, "A transformation for ordering multispectral data in terms of image quality with implications for noise removal," *IEEE Transactions on Geoscience and Remote Sensing*, **26**, no. 1, pp. 65–74, 1988.

Griffin, M.K., S. Hsu, H.K. Burke and J.W. Snow, "Characterization and delineation of plumes, clouds and fires in hyperspectral images," AeroSense, Orlando, FL, April 24–28, 2000.

Griffin, M.K., H.K. Burke, D. Mandl, and J. Miller, "Cloud Cover Detection Algorithm for EO-1 Hyperion Imagery," in Proceedings of SPIE Vol. 5093 *Algorithms and Technologies for Multispectral, Hyperspectral, and Ultraspectral Imagery IX*, edited by Sylvia S. Shen, Paul Lewis, (SPIE, Bellingham, WA, 2003), pp. 483–494.

Hsu, S., H.K. Burke, S. Orloff, and M. Griffin, "Examples of EO-1 Data Analysis," in Proceedings of SPIE Vol. 5093 *Algorithms and Technologies for Multispectral, Hyperspectral, and Ultraspectral Imagery IX*, edited by Sylvia S. Shen, Paul Lewis, (SPIE, Bellingham, WA, 2003).

IOCCG, "Minimum Requirements for an Operational, Ocean-Color Sensor for the Open Ocean," Reports of the International Ocean-Color Coordination Group (IOCCG) Report Number 1, 1998.

IOCCG, "Status and Plans for Satellite Ocean-Color Missions: Considerations for Complementary Missions," Reports of the International Ocean-Color Coordination Group (IOCCG) Report Number 2, 1999.

IOCCG, "Remote Sensing of Ocean Color in Coastal, and Other Optically-Complex, Waters," Reports of the International Ocean-Color Coordination Group (IOCCG) Report Number 3, 2000.

Keshava, N. and J.F. Mustard, "Spectral unmixing," *IEEE Signal Processing Magazine*, vol. 19, no. 1, pp. 44–57, January 2002.

Liew, S.C., "Computation of Coastal Sea Water Absorption Coefficients and Retrieval of Water Quality Parameters from EO-1 Hyperion Data," *IEEE IGARSS*, 2002.

Musick, H.B. and R.E. Pelletier, "Response of some thematic mapper band ratios to variation in soil water content," *Photogrammetric Engineering and Remote Sensing*, vol. 52, pp. 1661–1668, October 1986.

O'Reilly, J.E., M. Stephane, B.G. Mitchell, D.A. Siegel, K.L. Carter, S.A. Garver, M. Kahru and C. MacClain, "Ocean Color Chlorophyll Algorithms for SeaWiFS," *J. Geophy. Res.*, **103**, C11, pp. 24, 937–24,953, 1998.

Pearlman, J., S. Carman, C. Segal, P. Jarecke, and P. Barry, "Overview of the Hyperion Imaging Spectrometer for the NASA EO-1 Mission," *Proceedings of IGARRS 2001,* Sydney, Australia, 2001.

Richards, J.A., Remote Sensing Digital Image Analysis, Springer_Verlag, 1994.

Tucker, C.J., "Red and Photographic Infrared Linear Combinations for Monitoring Vegetation," *Remote Sens. Environ.*, **8**, pp. 127–150, 1979.

Ungar, S.G., "Overview of The Earth Observing One (EO-1) Mission," IEEE 2002.

REPORT DOCUMENTATION PAGE

Form Approved
OMB No. 0704-0188

1. REPORT DATE *(DD-MM-YYYY)*	2. REPORT TYPE	3. DATES COVERED *(From - To)*
12 January 2005	Project Report	

4. TITLE AND SUBTITLE

Examples of EO-1 Hyperion Data Analysis

5a. CONTRACT NUMBER
F19628-00-C-0002

5b. GRANT NUMBER

5c. PROGRAM ELEMENT NUMBER

6. AUTHOR(S)
M.K. Griffin, S.M. Hsu, H-h.K. Burke, S.M. Orloff, C.A. Upham, B. Misra

5d. PROJECT NUMBER

5e. TASK NUMBER

5f. WORK UNIT NUMBER

7. PERFORMING ORGANIZATION NAME(S) AND ADDRESS(ES)

MIT Lincoln Laboratory
244 Wood Street
Lexington, MA 02420-9108

8. PERFORMING ORGANIZATION REPORT NUMBER

HTAP-21

9. SPONSORING / MONITORING AGENCY NAME(S) AND ADDRESS(ES)
Department of the Under Secretary of Defense, S&T
Rosslyn Plaza North, Suite 9030
1777 N. Kent Street
Rosslyn, VA 22209

10. SPONSOR/MONITOR'S ACRONYM(S)

11. SPONSOR/MONITOR'S REPORT NUMBER(S)
ESC-TR-2004-081

12. DISTRIBUTION / AVAILABILITY STATEMENT

Approved for public release; distribution is unlimited.

13. SUPPLEMENTARY NOTES

14. ABSTRACT

The EO-1 satellite is part of NASA's New Millennium Program (NMP). It consists of three imaging sensors: the multispectral Advanced Land Imager (ALI), Hyperion, and Atmospheric Corrector. Hyperion provides a high-resolution hyperspectral imager capable of resolving 220 spectral bands (from 0.4 to 2.5 micron) with a 30-m resolution. The instrument images a 7.5 km by 100 km land area per image. Hyperion is currently the only space-borne HSI data source since the launch of EO-1 in late 2000.

A cloud-cover detection algorithm was developed for application to EO-1 Hyperion hyperspectral data. The algorithm uses only bands in the reflected solar spectral regions to discriminate clouds from surface features and was designed to be used on board the EO-1 satellite as part of the EO-1 Extended Mission Phase of the EO-1 Science Program. The cloud-cover algorithm uses only 6 bands to discriminate clouds from other bright surface features such as snow, ice, and desert sand. The technique was developed using 20 Hyperion scenes with varying cloud amount, cloud type, underlying surface characteristics, and seasonal conditions. Results from the application of the algorithm to these test scenes are given with a discussion on the accuracy of the procedure used in the cloud cover discrimination. Compared to subjective estimates of the scene cloud cover, the algorithm was typically within a few percent of the estimated total cloud cover.

15. SUBJECT TERMS

16. SECURITY CLASSIFICATION OF:			17. LIMITATION OF ABSTRACT	18. NUMBER OF PAGES	19a. NAME OF RESPONSIBLE PERSON
a. REPORT	b. ABSTRACT	c. THIS PAGE			19b. TELEPHONE NUMBER *(include area code)*
Unclassified	Unclassified	Unclassified	Same as report	64	